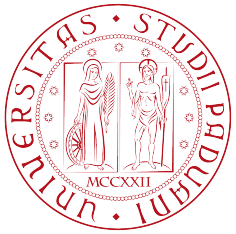

UNIVERSITÀ DEGLI STUDI DI PADOVA

Dipartimento di Fisica e Astronomia "Galileo Galilei"

Corso di Laurea in Fisica

Tesi di Laurea

Fermi LAT and the Observation of Flares in Extragalactic Sources

Relatore

Prof. Denis Bastieri

Laureanda

Francesca Bovolon

Anno Accademico 2017/2018

Contents

List of Figures

List of Tables

Preface

The detection of a high-energy neutrino by the IceCube Collaboration on September 22, 2017, followed by the observation of a possible optical counterpart (the flaring blazar TXS0506+056) by various ground-based and space-based observatories is the best hint so far to a simultaneous emission of neutrinos and photons from the same cosmic source. This could open the possibility of an experimental validation (or disproof) of current models on high-energy particle production in several astrophysical environments. Fermi Large Area Telescope (LAT) was the first collaboration to announce the observation of a potential counterpart to the IceCube neutrino event. There are many hypotheses now on the joint production of neutrinos and high-energy gamma rays by hadronic or lepto-hadronic interactions between accelerated particles in various sources, from flaring active galactic nuclei to supernova remnants. It is thus necessary assessing the probability that a concurrent detection of neutrinos and gamma rays from the same region in the sky, given that the neutrinos are astrophysical in nature, is indeed due to a common physical origin rather than to a mere coincidence. The first step is to study the space and time distribution of active gamma-ray sources. Known objects from the Fermi catalogs must be selected and their light curves reconstructed. Since building light curves for highly variable objects needs optimal time binning to guarantee the best statistical significance, variable bins must be used in turn. This has a much higher computational cost with respect to the fixed binning used for steady sources, so a good selection rule must be found to avoid wasting time and resources. After two introductory chapters on the Fermi Telescope and the current models on gamma-ray and neutrino production in active galactic nuclei, this thesis describes the data analysis performed on the September 22, 2017 event by various science collaborations and then tries to implement a selection criterion to pick the most variable extragalactic gamma-ray sources (mainly blazars, like TXS 0506+056) from the Third Fermi LAT Source Catalog (3FGL).

Chapter 1

The Fermi Gamma-ray Space Telescope

1.1 Introduction

The Fermi Gamma-ray Space Telescope (formerly GLAST, Gamma-ray Large Area Space Telescope) was designed, assembled and now maintained by a joint effort of NASA and various institutions in the United States, France, Italy, Japan and Sweden. Launched on June 11, 2008, it began full scientific operations on August 11, 2008 and is now completing its tenth year in orbit and its first extended mission.

Fermi was conceived as a successor to the Compton Gamma-Ray Observatory (CGRO), a NASA satellite for high-energy astrophysics in orbit from 1991 to 2000, whose results have provided a basis for Fermi's scientific work. One of the instruments on-board the CGRO, EGRET (Energetic Gamma-Ray Experiment Telescope), was a spark chamber detector of high-energy photons in the 30 MeV-30 GeV range. It observed a great variety of both Galactic and extragalactic sources and the background diffuse emission, performed the first all-sky survey at energies above 50 MeV and detected over 400 potential sources, 271 of which were included in the Third EGRET Catalog [21]. Most of them, however, remained unidentified, requiring further study. Among other objectives, Fermi was designed to determine their nature and expand on the discoveries made by the CGRO, thanks to a series of technological improvements adopted by the two instruments on board: the Large Area Telescope (LAT), EGRET's successor, and the Gamma-ray Burst Monitor (GBM), aimed at detecting transients.

The two instruments work together: when the GBM detects a potential gamma-ray burst, the onboard science processing system computes the burst position and communicates it to the LAT, triggering an autonomous re-pointing of the spacecraft if the burst fluency is above a given threshold and keeping the GRB in the LAT field of view for the next 5 hours; conversely, the LAT software can send the GBM orders. The information on the event is also sent to the ground, allowing for requests of further ground- or space-based observations through the GRB Coordinates Network / Transient Astronomy Network[1]. When Fermi is not pointed towards a particular target, it observes the sky in "scanning" or "rocking" mode, to take full advantage of its large field-of-view: the normal to the front of the instrument is pointed to 0°-60° from the zenith and towards the pole of the orbit on

[1] See `https://gcn.gsfc.nasa.gov/` The network links various institutions and observatories in the fields of high-energy astrophysics, astroparticle physics and gravitational physics: INTEGRAL, Swift, AGILE, the MAXI and CALET instruments on board the International Space Station, MOA, LIGO/Virgo, and the SNEWS network of neutrino observatories, including IceCube.

alternate orbits, and in the opposite direction from the zenith on the subsequent orbits. As a consequence, after 2 orbits (about 3 hours) the sky exposure is almost uniform. Fermi moves on a low Earth orbit at about 565 km, with an inclination of 25.6°. The chosen altitude allows the satellite to stay below the inner Van Allen radiation belt, except when it transits inside the South Atlantic Anomaly, where the charged particles background is so intense that the LAT is forced to stop taking data.

1.2 Technical description

1.2.1 The Gamma-ray Burst Monitor

Fermi's secondary instrument, the Gamma-ray Burst Monitor (GBM) is a set of scintillator detectors whose main role is to complement the LAT in its observation of the higher-energy component of gamma-ray bursts. The GBM detects photons at lower energies (8 keV-40 MeV) with respect to the LAT, thus extending to 7 decades the energy range of burst spectra provided by the telescope. The GBM is also triggered by other types of transients, providing data on solar flares, soft gamma repeaters and terrestrial gamma flashes, in addition to background data which are used in a wide variety of studies.

The GBM consists of a Data Processing Unit, a power box and two sets of scintillation detectors, mounted on opposite sides of the spacecraft to guarantee that any burst above the horizon would be visible. Each set comprises one BGO detector to measure the higher-energy spectrum (0.2 MeV to 40 MeV), allowing cross-calibration with the LAT, and six NaI(Tl) detectors to measure the low-energy spectrum (8 keV to 1 MeV) and determine the direction of the burst by comparing the count rates of detectors mounted at different viewing angles.

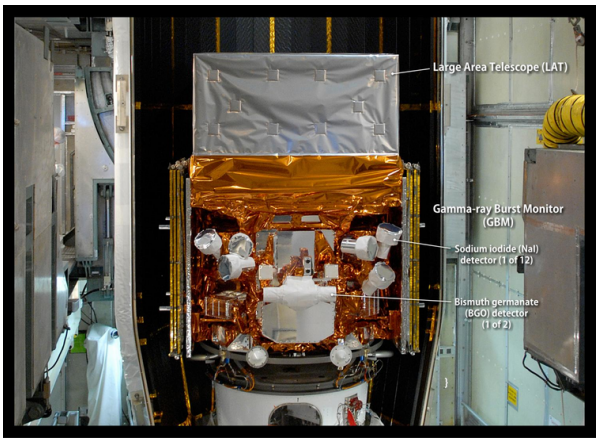

(a)

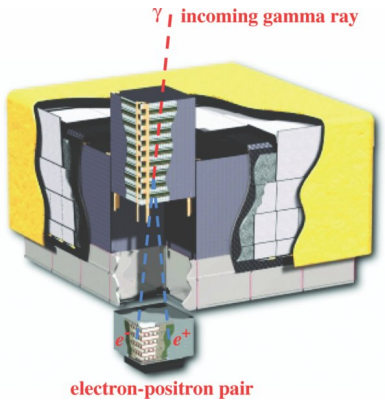

(b)

Figure 1.1: (a) The Fermi spacecraft inside the payload fairing shortly before launch. Credit: NASA/Jim Grossmann. (b) Cutaway view of the Large Area Telescope [10].

1.2.2 The Large Area Telescope

Fermi's primary instrument is the Large Area Telescope (LAT), a wide field-of-view imaging telescope able to detect photons in the energy range $\sim$ 20 MeV-over 300 GeV. It can rely on:

- high sensitivity on a larger field-of-view (due to a larger effective area[2] and a low aspect ratio of 0.4) to better monitor source variability and transients;
- improved particle tracking, allowing for a good angular resolution and background rejection for source localization and multi-wavelength studies;
- good calorimetry over a large energy band, to improve the spectral representation of sources;
- overall stability and good calibration, for absolute and long-term photon flux measures;
- a faster ad more efficient trigger and data acquisition system with a low readout deadtime to better study variability and transients.

All these needs have been met thanks to a long and careful development phase, which included detailed simulations of the instrument response, the choice of well-established technology to guarantee reliability, and the study of test models.

Parameter	Value or Range
Energy range[a]	$20\,\mathrm{MeV} - 3\,\mathrm{TeV}$
Effective area at normal incidence (total)	$> 9000\,\mathrm{cm}^2$ (10 GeV)
Weighted energy resolution (total, 68% containment; on-axis):	
100 MeV-1 GeV	$\sim 19.5\% - 10\%$
1 GeV-10 GeV	$\sim 10\% - 6.5\%$
10 GeV-300 GeV	$\sim 6.5\% - 8.5\%$
1 TeV	$>12\%$
Acceptance-weighted PSF (total), 68% containment angle:	
100 MeV	$\sim 5^\circ$
1 GeV	$\sim 0.8^\circ$
10 GeV	$< 0.2^\circ$
1 TeV	$\sim 0.08^\circ$
Field of View	2.4 sr
Timing accuracy	300 ns
Single event readout time (dead time)	26.5 µs

[a] The Instrument Response Functions (IRFs) available publicly allow only the handling of data between 100 MeV and 1 TeV.

Table 1.1: Performance characteristics of the Fermi LAT (Pass 8 data release). See [42]

Gamma rays are detected exploiting the interaction they have with matter, primarily by conversion into an e^+e^- pair[3]. The LAT is thus a pair-conversion telescope with a precision converter-tracker and a calorimeter. Each of these two sections consists of a 4×4 array of 16 modules supported by an aluminium grid, and a segmented anticoincidence detector (ACD) covers the tracker. A programmable trigger and data acquisition system (DAQ) uses signals from the tracker, the calorimeter and the ACD to form a multilevel trigger, which initiates the readout of the three sections and the on-board signal processing before sending the data to the ground in the case the event is not rejected as background. The

[2] $FoV = \int A_{\mathrm{eff}}(\theta,\phi)d\Omega / A_{\mathrm{eff}}(0,0)$. A_{eff} is the effective area, which can be defined as the number of detected photons with respect to the source flux, and is a function of photon energy and incidence angle.

[3] Pair production is possible for $E > 1.02\,\mathrm{MeV}$ and predominant for energies above $\sim 5\,\mathrm{MeV}$ at high Z. See [27], pp. 51-52

upper part of the telescope is wrapped in a multilayer thermal and anti-micrometeoroid shield to protect the ACD from damage and light leaks. The whole instrument is 1.8 m square and 0.72 m deep and has a mass of 2789 kg.

The converter-tracker The converter-tracker of the LAT employs AC-coupled silicon-strip detectors (SSDs) as active elements. They are self-triggering, durable and permit a low aspect ratio. This is a great advantage with respect to EGRET, whose tracking section was a spark chamber and thus relied on a consumable substance (gas) and an external trigger based on the time-of-flight principle. Each tracker module consists of 18 x, y tracking planes, each made of two layers of n-intrinsic, single-sided silicon strips. The upper 16 planes are interleaved with tungsten ($Z = 74$) converter foils[4]. Sets of 4 SSDs are bonded edge-to-edge and then wire-bonded strip to strip. 4 such strips form one detector layer in one module. Silicon-strip layers, converter foils and front-end electronics are housed in a structure of 19 trays supported by sidewalls which also conduct heat to the base of the tracker. The strips on the top and bottom of each tray are parallel, while alternate trays are rotated 90° relative to each other, so that a x, y measurement plane consists of the SSD on the bottom of one tray and the SSD on top of the tray just below. The converter foils in the top 16 planes lie above the upper layer in each plane.

The tracker has been designed to optimize the event reconstruction, avoiding particle energy loss in the detector as much as possible. The Point Spread Function (PSF) gives the probability distribution for the reconstructed direction of incident gamma rays from a point source and therefore describes the instrument resolution. Many factors influence the PSF and have been taken into consideration while developing the LAT. The tracker is built to maximize the conversion of gamma rays into electron-positron pairs inside the tungsten foils, the detection of pairs in the first layer immediately below the converter foil, and the separate detection of the two tracks produced by each pair. Consequently, the detector is finely segmented, inactive elements are minimized, and the silicon strips have high efficiency and lie very close to the tungsten foils, which in turn cover only the active areas of the SSDs to reduce the probability of "missing hits" (e^-e^+ couples not immediately detected by the first layer following the conversion). This allows for a better background rejection and reduces the resolution degradation due to Bremsstrahlung and multiple scattering. The PSF depends on energy, thus thin converters are required at low energies to avoid multiple scattering, but thicker ones at high energies to maximize the effective area. This has led to dividing the tracker into two regions: the "Front" (first 12 tracking planes, with 0.03 radiation lengths thick tungsten foils) and the "Back" (13th to 16th tracking planes, with thicker foils; the last 2 planes have no converters). The performance of the LAT is further enhanced by its readout electronics, which achieve high throughput and very low deadtime (thanks to the ability of buffering events), contribute to background rejection, produce a compact output with very low noise occupancy, and need little calibration. The readout system is mainly triggered by the tracker itself when a coincidence of successive planes occurs; the trigger efficiency approaches 100%. Lastly, the LAT is characterized by high reliability, guaranteed by the use of independently working components.

The calorimeter The main purposes of the calorimeter are to measure the total energy of the incoming photon, estimate the leakage fluctuations, which affect the energy resolution, and provide further data for background rejection. Each module consists of 96

[4] A high-Z element increases the pair production probability per nucleus, which approximately varies as Z^2. ([27], p. 52)

optically isolated CsI(Tl) crystals, arranged horizontally in 8 layers of 12 crystals each, for a total depth of 8.6 radiation lengths[5]. The layers are rotated 90° with respect to each other to form a hodoscopic configuration, which allows to image the electromagnetic shower generated by the e^-e^+ pair. The provided spatial coordinates can complement the tracker data to better reconstruct the direction of the incident photon. The segmentation enables energy measurements up to at least a TeV: the imaged longitudinal shower profile is fitted to an analytical model of the energy-dependent mean profile to estimate the initial electron energy.

At both ends of each crystal, PIN photodiodes measure the scintillation light which is transmitted to each end; the difference in light levels allows to reconstruct the energy deposition along the crystal. There are two photodiodes at each end of the crystal: a large one ($147\,\mathrm{mm}^2$ area, for energy deposition between 2 MeV and 1.6 GeV) and a small one ($25\,\mathrm{mm}^2$ area, energy deposition 100 MeV-70 GeV), each providing one independent readout channel through its own front-end electronics.

The anticoincidence detector The role of the anticoincidence detector (ACD) is to provide background rejection by detecting charged cosmic particles that enter the field-of-view of the LAT, and generating a veto signal. Its efficiency in detecting single-charged particles must therefore be at least 0.9997. The ACD must also handle the backsplash effect, which could affect photon detection efficiency. Secondary particles (mostly $100 - 1000$ keV photons) from the shower generated in the heavy calorimeter can Compton scatter in the lower planes of the tracker and in the ACD, creating a spurious veto signal ("self-veto") from the recoil electrons. This phenomenon was a strong limiting factor in EGRET, which featured a monolithic ACD. The LAT ACD is segmented, so that only the response from the segments near the incident candidate photon is considered. Moreover, the ACD vetoes are ignored every time the energy deposition in the calorimeter exceeds a certain threshold, so that all the data can be sent to the ground to be analyzed more thoroughly.

The ACD segments are 89 plastic scintillator tiles, in which wavelength shifting fibers (WLS) are embedded. Detection efficiency is maintained by overlapping tiles in one dimension; in the other dimension, the gaps are filled by 8 scintillating fiber ribbons. This arrangement provides over 95% light collection uniformity over each tile near the centre. A combination of wavelength-shifting and clear fibers delivers scintillation light from the tiles and WLS to two photomultiplier tubes and to the electronics.

The data acquisition system and the trigger The LAT includes a multi-purpose data acquisition system (DAQ) which collects the data from the other subsystems, filters them, performs some on-board analysis to rapidly deal with transients, and implements the trigger. It has a hierarchical structure:

1. The Tower Electronics Modules (TEMs) are the interfaces to each of the 16 tracker-calorimeter modules. They generate first-level triggers, provide event buffering and communicate with upper-level electronics.

2. The GASU (Global-trigger/ACD-module/Signal distribution Unit) consists of 4 modules:

   - the Command Response Unit (CSU), which handles commands and distributes the clock signal;

[5]The total depth of the LAT is 10.1 radiation lengths.

- the Global-trigger Electronics Module (GEM) that combines the trigger and veto signals from the TEMs and the ACD into a global trigger;
- the ACD Electronics Module, which performs the same tasks of the TEMs for the ACD;
- the Event Builder Module (EBM), which builds complete LAT events and sends them to the Event Processor Units.

3. The two Event Processor Units (EPUs) apply filter algorithms to remove background events and maximize the rate of "good" gamma-ray events with respect to the total rate that can be downlinked ($\sim 400\,\mathrm{Hz}$).

4. The Spacecraft Interface Unity (SIU) controls the LAT and contains the command interface to the spacecraft.

The trigger system consists in an exchange of requests and accept messages between the TEMs or the AEM and the GEM when particular conditions are met: 3 x, y planes in a row are activated in the tracker, or certain thresholds are exceeded anywhere in the calorimeter or ACD. The instrument minimum deadtime per event readout is $26.5\,\mu\mathrm{s}$, which is the time needed to elaborate the global trigger signal in the GEM and send it to the EBM. It is a great improvement over the EGRET trigger, whose spark chamber deadtime was $\sim 100\,\mathrm{ms}$.

1.2.3 Event reconstruction and background rejection

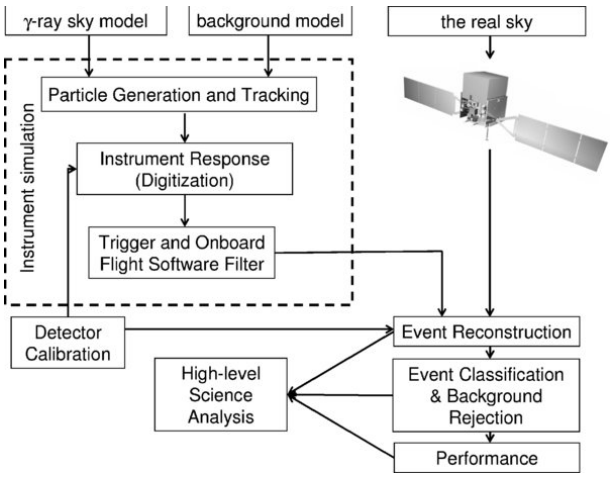

Figure 1.2: Components of the instrument simulation, calibration, and data analysis. [10]

The LAT performance and response has recently been improved with the introduction of Pass 8, a complete rework of the event reconstruction framework which specifically addresses some neglected issues (ghost signals in the calorimeter, multiple scattering in the tracker, multiple hits in the SSDs) that emerged during the active phase of the mission [11]. Event-level analysis comprises three main areas: Monte Carlo modeling of the instrument, event reconstruction and background rejection.

Old techniques (calorimeter-seeded pattern recognition and blind search pattern recognition) implied locating track candidates, populating them with hits to find the best fits and combining them to find a vertex. The new global "tree-based tracking" considers e^-e^+ interaction more as a shower, or tree. The result is then matched to calorimeter and ACD data and the best tracks extracted and fitted. If two tracks are produced from a

tree, they are combined to find the pair conversion vertex. The calorimeter reconstruction has been improved as well by switching from a "monolithic" energy deposit model to a "clustered" one, in order to account for ghost signals. Moreover, single crystal signals are now considered, allowing for a decent energy resolution up to $\sim$3 TeV. Background rejection by the ACD takes into account both tracker and calorimeter information. After the track and energy reconstruction, event candidate probabilities are sorted in "Classification Trees" on the basis of reconstruction outputs, and evaluated. To improve the instrument response and extend the scientific reach of the instrument, uncertainties are evaluated event-by-event and many types of events are considered: multi-photon, tracker-only, calorimeter-only and Compton scattering events are also accepted in addition to single-photon tracker-plus-calorimeter ones. The final step is background rejection; most of the triggers, and therefore most of the downlinked events, are indeed due to background. Both onboard filtering and analysis on the ground rely on cosmic-ray background models developed from data collected by other experiments (the AMS series, BESS, Pamela, the NINA series, Mariya, EGRET). Reconstructed events are filtered on the basis of the track topology, using different criteria depending on the event class: Transient, Source or Diffuse.

1.3 Observations and results

Galactic and extragalactic diffuse emission One of the main scientific objectives addressed by Fermi is to improve the knowledge of diffuse gamma-ray emission. The Galactic component is thought to be generated by the interaction between energetic cosmic rays and the interstellar medium (primarily via Bremsstrahlung and π^0 production and decay) or interstellar radiation fields (via inverse Compton scattering). Studying it, in addition to improve the background model to better resolve point sources and detect the extragalactic diffuse emission, allows to inspect the acceleration, propagation and spectra of cosmic rays and to map the interstellar medium. The so-called "EGRET GeV excess" has been discredited, but a surplus emission has indeed been observed both around the Galactic center and in the outer regions of the Galaxy, hinting at new models of the Milky Way. The Fermi LAT has also observed structures in the Galactic diffuse emission, such as the "Fermi bubbles", two giant high-energy (> 6.4 GeV) lobes extending above and below the Galactic center, probably created by inverse Compton scattering of low-energy photons by electrons accelerated during a period of increased nucleus activity millions of years ago.

The isotropic, extragalactic component of the diffuse emission (extragalactic background, EGB) is a sum of two contributions: unresolved point sources and truly diffuse emission. LAT obtained a spectrum compatible with extragalactic point sources, therefore suggesting that the EGB is mainly due to them. The spectral analysis of EGB with LAT data is the first in the 100 MeV $-$ 820 GeV range.

Dark matter The observation of the diffuse gamma-ray background is strongly tied to the search of dark matter as WIMPs (Weakly Interacting Massive Particles), whose annihilations and decays may produce ordinary particles, such as gamma-ray photons. It is not sure if Fermi could detect them, but the LAT instrument still contributes to the quest. As already mentioned, Fermi has observed a spherically symmetric excess of GeV emission near the Galactic center, as predicted by some dark matter models. However, it could be due to flaws in the model of Galactic diffuse emission, or to ordinary astrophysical reasons. Fermi also studies dwarf spheroidal galaxies, galaxy clusters and the extragalactic diffuse background. While the observation of galaxy clusters still has no outcome, focusing on the other two sources has provided some of the most constraining limits on the dark

matter annihilation cross section.

Pulsars, plerions and supernova remnants Pulsars were the only Galactic sources positively identified by EGRET. The development of algorithms to find periodicity in gamma-ray data and the technical improvements brought about by the LAT have led to the discovery of two orders of magnitude more gamma-ray pulsars. Gamma-ray emission originates in non-thermal processes (curvature radiation, synchrotron radiation and inverse Compton scattering) in the magnetospheres of neutron stars, where rotation-induced electric fields accelerate charged particles to at least 10 TeV. Phase-averaged spectra obtained from LAT data have supported the "outer gap" model, according to which $\gamma + \gamma \rightarrow e^- + e^+$ interactions occur in the outer magnetosphere of the pulsar. Millisecond pulsars are a class of neutron stars whose knowledge has greatly improved thanks to Fermi[6]; some of them have also been found in globular clusters, whose gamma-ray emission had never been detected before.

Apart from electromagnetic radiation, pulsar spin-down power is lost through magnetized winds of charged particles, forming a pulsar wind nebula (PWN), or plerion. Here particles are accelerated and generate gamma-rays from synchrotron radiation and inverse Compton scattering. While PWNs are the dominant sources at TeV energies, Fermi has observed GeV emission from a number of them. An interesting discovery is the short-term variability of the Crab Nebula, which has been shown to flare instead of being a stationary source as believed before.

Data from Fermi and ground-based observatories have confirmed that Galactic, lower-energy ($<10^{15}$eV) cosmic rays are produced by acceleration of particles in the expanding shocks of supernova remnants interacting with the surrounding medium. The LAT has found the signature of π^0 decay in the spectra of some SNRs, confirming that leptonic and hadronic gamma-ray emission mechanisms can be distinguished.

Binary sources The Fermi LAT has detected gamma emission from a variety of Galactic binary systems, many of which are high-mass X-ray binaries (HMXBs). The LAT has detected an orbitally modulated emission from some neutron star binaries, where gamma rays are produced via inverse Compton scattering by pulsar winds colliding with the stellar wind or the companion star disk near the periastron. Fermi has also observed one microquasar, Cygnus X-3, whose gamma-ray flares are generated by particle acceleration in the only Galactic relativistic jet detected by the satellite so far. Finally, the LAT has been the first instrument to detect gamma-ray emission from optical novae.

Local sources As expected, Fermi has been able to inspect gamma-ray emission from the Solar System. The LAT has detected the most energetic ($\sim$ 4 GeV) photons ever observed from a solar flare. It has also observed gamma-ray emission from interaction of the quiescent Sun and the Moon with cosmic rays. For the same reason, the Earth limb[7] is a strong source of diffuse gamma rays, but also of "gamma-ray flashes" and electron and positron beams associated with lightning.

Normal and starburst galaxies The same processes governing cosmic-ray interactions operate also in other normal galaxies, some of which (the Magellanic Clouds, the Andromeda galaxy) have indeed been detected by Fermi as gamma-ray sources. So-called

[6] The first gamma-ray only millisecond pulsar has recently been discovered by the crowd computing project Einstein@Home using Fermi data [15].

[7] The portion of the Earth falling into the Fermi LAT's field-of-view.

starburst galaxies feature high supernova-explosion and star-formation rates and great gas mass, dust mass and photon densities that make them good sources to test theories on cosmic ray production.

Active galaxies Active galaxies (blazars, radio galaxies, Seyfert galaxies) are by far the most abundant class of gamma-ray sources in the extragalactic sky as observed by the Fermi LAT. The Third Fermi Gamma-ray Catalog (3FGL) is the largest catalog of gamma-ray detected AGN ever made, featuring 1563 associated sources of this kind, most of which are blazars. Population and spectral studies of AGNs allow to estimate the contribution of these objects to the extragalactic gamma-ray background. Analysis of light curves (variability) and of spectra on a wide energy range, in addition to comparisons with data at other wavelengths, can give new information on the growth and evolution of supermassive black holes, test the unified model and unravel the physics of relativistic jets. While some observations have corroborated previous results by EGRET, some unexpected findings are challenging the models. Some high-luminosity blazars show a broken power-law spectrum which, according to some interpretations, would be inconsistent with the measurements at longer wavelengths. Some gamma-ray flares point, when compared to their radio counterparts, to mechanisms which are not predicted by current descriptions of AGN physics. The unforeseen observation of high-energy emission from a small number of radio-loud narrow-line Seyfert 1 galaxies questions the current unification model. Fermi has also detected periodic variability in at least one source, opening up the possibility that some AGNs could be binary systems of supermassive black holes.

Gamma-ray bursts Before the launch of Fermi, little was known about the higher-energy emission of GRBs and the time structure of their prompt component. In addition to constantly providing new data on the physical mechanisms behind these explosions, the GBM was the first instrument to detect and signal the neutron star merger event of August 17, 2017 (GRB 170817A), confirming the kilonova hypothesis about short-duration ($\tau < 2\,\mathrm{s}$) GRBs. Long-duration GRBs have instead been shown to originate from some core-collapse supernovae (Type Ibc). The exact mechanism of burst birth and development, however, is still debated following some important results from Fermi. Generally speaking, a prompt gamma-ray and X-ray emission from the initial super-relativistic blast is followed by a hours- or even months-long afterglow at lower energy bands, generated via interaction of the ejecta with the interstellar medium. Observations with the LAT ($\sim 10/year$) have highlighted a slight delay of the GeV emission with respect to lower-energy gamma and X rays detected by the GBM, a long-lasting emission at energies above 100 MeV (sometimes even reaching 95 GeV), and a new high-energy spectral component.

Since GRBs happen at cosmological distances and generate photons on a wide range of energies, Fermi data are really important in testing Lorentz invariance and putting constraints on the quantum gravity mass scale. Experimental measures of the speed of gamma-ray photons have so far confirmed Lorentz invariance.

Extragalactic background light The Extragalactic background light (EBL) is a residual accumulated radiation from star and structure formation. Fermi allows to investigate it in the almost unexplored optical-UV band. Gamma-ray photons above 10 GeV coming from distant AGNs can be absorbed by the EBL through e^-e^+ pair production, creating distinct features in the spectra of active galaxies. The absorption has been shown to increase with distance, and thus with cosmological redshift, reflecting the trend of star formation throughout the history of the Universe.

Cosmic electrons and positrons Charged particles detection for background rejection allows to measure cosmic electron and positron spectra from 7 GeV to 2 TeV and compare them with results from other experiments, like H.E.S.S. and AMS-02.

1.3.1 Fermi and multimessenger astrophysics

In these years, Fermi has been providing valuable material for the newborn field of *multi-messenger astrophysics*. Thanks to the discoveries of high-energy astrophysical neutrinos [1] and gravitational waves [5] some cosmic phenomena can now be observed through new channels in addition to the "traditional", optical one. As already mentioned, the Fermi GBM was the first instrument to signal the neutron star merger of August 17, 2017 [6], whose simultaneous detection of a gravitational wave followed by a large number of other observations in the electromagnetic spectrum marked the first truly multimessenger study of an astrophysical phenomenon. The detection of a candidate cosmic neutrino by the IceCube Observatory on September 22, 2017 was followed by the finding of a possible gamma-ray counterpart, the flaring blazar TXS 0506+056, by the Fermi LAT Collaboration. Since no previous occurrence of a spatial coincidence between a neutrino and a gamma-ray source had been so striking, confirming the correlation would pave the way for an all-inclusive description of particle acceleration and cosmic-ray production in objects like AGNs.

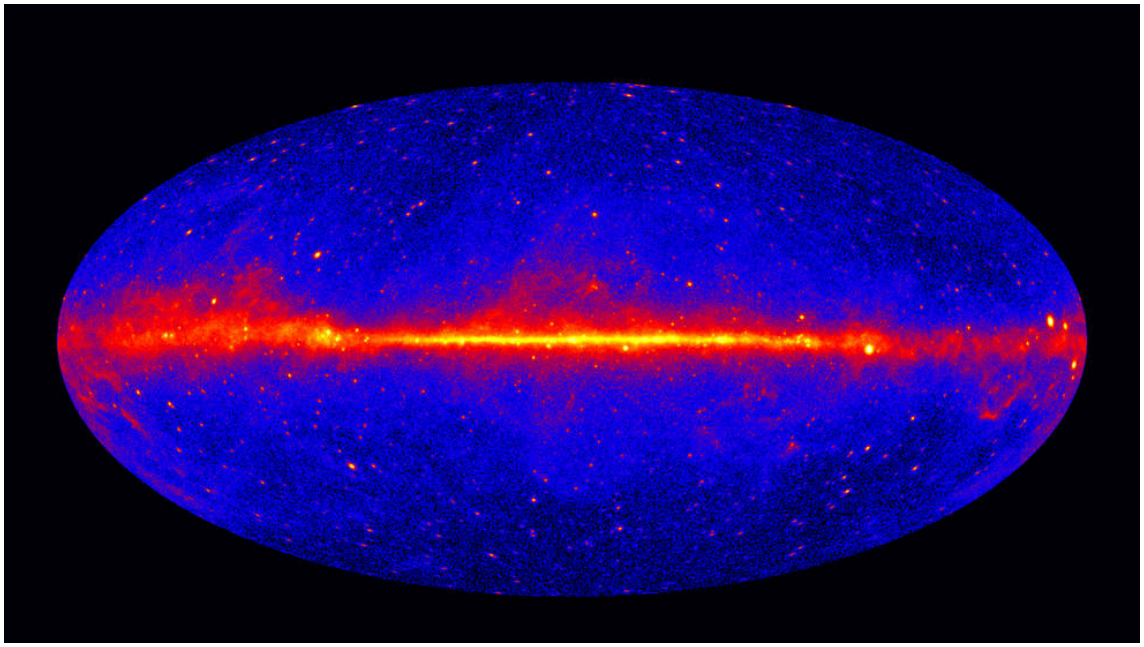

Figure 1.3: All-sky map at energies above 1 GeV, obtained from 60 months of Fermi LAT data. Galactic coordinates, Hammer-Aitoff projection. Credit: NASA/DOE/Fermi LAT Collaboration.

Chapter 2

Active Galactic Nuclei and Neutrinos

Despite extensive observations in the full electromagnetic spectrum, the physical processes happening in some cosmic high-energy sources like Active Galactic Nuclei are not fully understood yet. Models describing them are constantly being updated by new results yielded by missions like Fermi, confirming that much has still to be done to get the full picture of how supermassive black holes and relativistic jets behave, and how high-energy particles like gamma-ray photons and cosmic rays are produced and accelerated. A great step forward would be done with the concurrent observation of the other particles generated in these mechanisms: high-energy neutrinos. Since they are not subject to electromagnetic interactions, neutrinos can travel from their distant birthplaces to Earth unimpeded, thus giving unbiased information on their sources.

2.1 Neutrino- and photon-producing interactions

Astrophysical gamma rays are produced in several types of interaction between relativistic particles and matter or radiation fields. A prominent role is played by leptonic processes, such as synchrotron and curvature radiation from extremely energetic particles accelerated in strong magnetic fields, or inverse Compton scattering (in which relativistic electrons are scattered on soft photons, transferring to them their kinetic energy). However, gamma-ray production is also possible via hadronic processes, in which protons interact to produce pions, in their turn decaying into lighter particles like photons and neutrinos, that could therefore be detected in coincidence. The so-called *astrophysical beam dump* mechanism takes the form:

$$p + p \rightarrow \pi^{\pm}, \pi^{0}, K^{\pm}, K^{0}, \ldots \tag{2.1}$$

where "..." may be higher mass particles. Pions can alternatively be produced by *photo-production* in regions of high density of synchrotron *ambient photons* at radio-UV energies:

$$p + \gamma \rightarrow \pi^{0} + p \quad \text{or} \quad p + \gamma \rightarrow \pi^{+} + n \tag{2.2}$$

The products then decay:

$$n \rightarrow p + e^{-} + \bar{\nu_e} \tag{2.3}$$

$$\pi_0 \rightarrow 2\gamma \tag{2.4}$$

$$\pi^{+} \rightarrow \mu^{+} + \nu_\mu \quad \text{or} \quad \pi^{-} \rightarrow \mu^{-} + \bar{\nu_\mu} \tag{2.5}$$

$$\mu^{+} \rightarrow e^{+} + \nu_e + \bar{\nu_\mu} \quad \text{or} \quad \mu^{-} \rightarrow e^{-} + \bar{\nu_e} + \nu_\mu \tag{2.6}$$

These different photon production channels should be detectable by the shape of the spectral energy distribution (SED) of a source, sometimes even in the absence of a neutrino

counterpart (for example, Fermi observations of supernova remnants IC443 and W44 have identified the signature of neutral pion decaying).

2.2 Active Galactic Nuclei

Active Galactic Nuclei (AGNs) are at the center of inquiries on high-energy cosmic ray, gamma ray and neutrino production. These objects are variously classified according to their characteristics as observed at radio and optical wavelengths. A first subdivision is between radio-quiet and radio-loud sources. The emission of radio-weak sources is mostly dominated by thermal radiation and inverse Compton scattering. Most of these AGNs are classified as *Seyfert galaxies* or *radio-quiet quasars*. On the other hand the emission in radio-loud AGNs is mainly due to non-thermal interactions. These objects can be grouped into:

- *Blazars*. This broadly defined category includes AGNs with a flat radio spectrum, a polarized optical and/or radio emission and a significant variability. Main subcategories are:
  - *Flat Spectrum Radio Quasars (FSRQs)*. Doppler-broadened optical emission lines are recognizable over the non-thermal spectral continuum.
  - *BL Lacertae objects (BL Lacs)* Their spectra lack emission or absorption lines. Fermi data have shown that the average GeV gamma-ray spectra of BL Lacs are significantly harder than the spectra of FSRQs.
- *Nonaligned blazars*. This category comprises:
  - *Radio galaxies*. Active galaxies whose powerful radio emission is associated to relativistic jets ejected from their nuclei, often extending into giant radio lobes and hotspots.
  - *Steep Spectrum Radio Quasars (SSRQs)* characterized by broad emission lines.

Blazars can also be subdivided into three classes according to the position of the synchrotron-related peak in their SED: *low synchrotron peak* (LSP), *intermediate synchrotron peak* (ISP) and *high synchtrotron peak* (HSP). The majority of FSRQs are LSP blazars, while HSP blazars are mainly BL Lacs. Data analysis suggest a trend, despite few outliers, of a so-called "blazar sequence", in which the synchtrotron peak energy decreases with increasing blazar luminosity: FSRQ→LSP→ISP→HSP.

Current models describe unified scenarios both for radio-quiet and radio-loud AGNs, so that various classes can be traced to few object types (compact[1] galactic nuclei powered by a supermassive black hole) differing only in orientation, accretion rates, presence of relativistic jets and host galaxy class. Strong emission from the nuclear region of a galaxy (usually an elliptical one for radio-loud AGNs) is powered by the conversion of gravitational energy into kinetic energy of matter from an accretion disk falling into a supermassive black hole. Fast-moving ionized gas heated by the radiation from the disk produces the broad emission lines. The nucleus is surrounded by an optically thick dust and gas torus and farther and slower gas clouds (narrow-line region). Bipolar jets of plasma emanate at relativistic speed (bulk Lorentz factor $\Gamma \sim 50$ or higher) from the central region of radio-loud AGNs along the poles of the disk or torus. Different jet-dominated AGNs coincide with different points of view: if the object is looked at from a very large angle with respect

[1] "Compact" here means comparable to the Schwarzschild radius of the black hole.

to the jet axis, so that the torus obscures the optical and ultraviolet broad-line emission but the radio lobes are visible, a radio galaxy is observed. The jets of blazars are instead pointed almost exactly on the line of sight. This gives rise to relativistic effects like emission boosting and apparent superluminal motion of individual jet components propagating away from the core. Intermediate viewing angles let observers see radio-loud quasars.

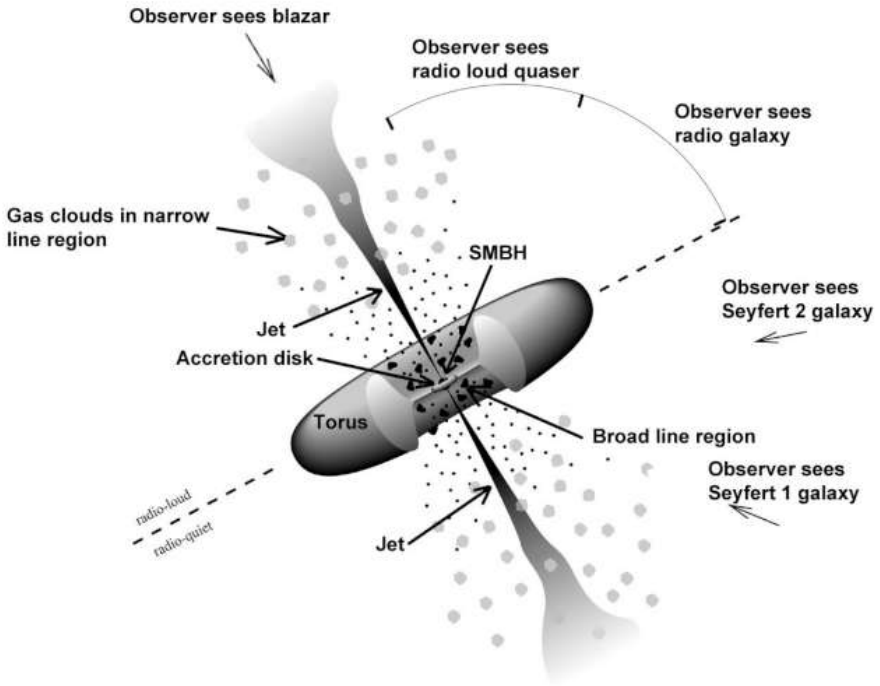

Figure 2.1: Unified model of AGNs. [18]

Insights on blazar structure and physical processes are given by its peculiar SED (Figure 2.7). Two very broad peaks are recognizable: one at lower energies (radio to X rays) and one from X rays upward. The lower-energy bump is thought to be due to synchrotron radiation from highly relativistic electrons, while the high-energy peak is described as the product of inverse Compton scattering of electrons on synchtrotron photons. *One-zone* leptonic synchrotron self-Compton well fits data for HSPs: a blob of plasma in a randomly oriented magnetic field interacts with an isotropic electron distribution and travels along the jet axis at relativistic speed. Instabilities in the plasma generate shocks which accelerate particles, producing photons whose flux is enhanced inside the jets. The fact that photons are carried inside a jet is necessary to explain observations, since a compact photon source would otherwise be opaque because of $\gamma - \gamma$ pair production. External Compton is needed to better fit the ISP SED. FSRQ spectra are instead better explained by a combination of leptonic and hadronic processes. This brings about difficulties, since leptonic and hadronic models match different physical scenarios and can be variously associated to different descriptions of the nuclear region, the jets and the strong magnetic fields involved; some models argue, for example, that magnetic fields may be highly ordered, but occasionally disrupted by flaring events. Polarization studies and correlations between gamma-ray and radio emission suggest that the processes generating gamma rays during flares do not happen in the inner region of the AGN as expected, but are associated to "radio knots", standing shocks situated 1-10 parsecs away from the black hole. Very-high-energy gamma-ray observations indicate that particles are accelerated at energies high enough to explain the production of ultra-high-energy cosmic rays by hadronic interactions in some

blazars, but the short-timescale variability of these sources is better explained by leptonic models. The occurrence of "orphan flares" at TeV lacking lower-energy counterparts hints at hadronic processes. Consequently, detecting neutrinos from AGNs is probably the only way to settle the dispute on hadronic interactions.

2.3 Finding astrophysical neutrinos with IceCube

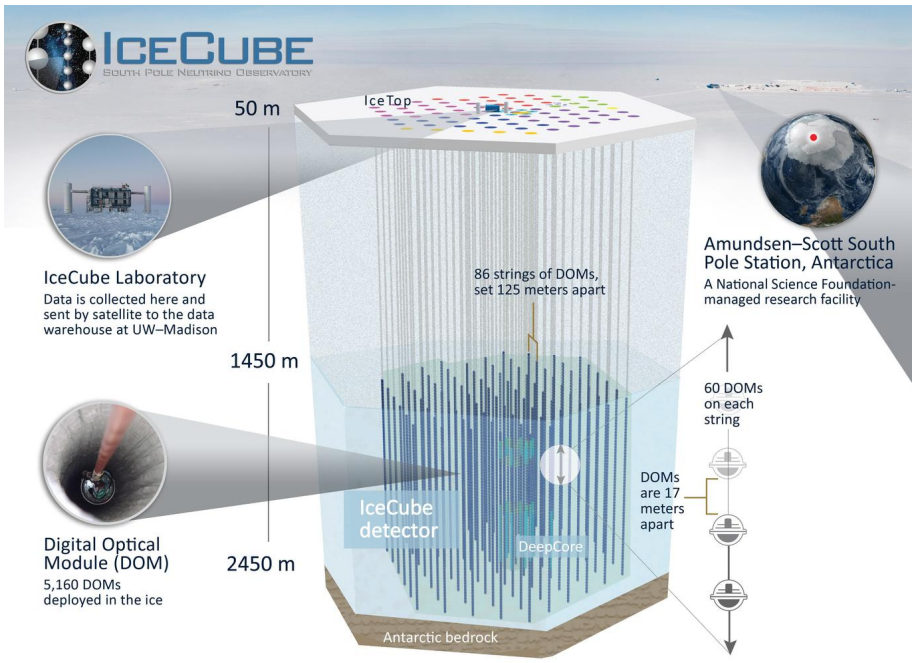

Figure 2.2: The IceCube facilities. Credit: IceCube Collaboration

The detector High-energy astrophysical neutrinos are currently studied by a small number of instruments (IceCube, ANTARES, Baikal Deep Underwater Neutrino Telescope) which employ large *instrumented volumes* of water or ice as active elements. The biggest is the IceCube Neutrino Observatory, a project run by the National Science Foundation, the University of Wisconsin-Madison and an international collaboration at the Amundsen-Scott South Pole Station. It began taking data in full configuration in 2011. It consists of three components: IceCube proper, IceTop and DeepCore. The primary detector is a hexagonal array of 78 vertical strings, each supporting 60 Digital Optical Modules (DOMs) composed of a photomultiplier tube, its electronic readout, and LEDs for calibration. The mean distance between strings is $\sim 125\,\mathrm{m}$, while DOMs along each string are 17 m apart. The lower part of the detector volume is more densely instrumented and forms a section called DeepCore, which is optimized for energies of a few tens GeV. IceTop is a surface array of 162 tanks filled with ice, arranged in pairs and equipped with two DOMs each. It acts as a veto and calibration cosmic-ray air shower detector in coincidence with IceCube. The main instrument sensors lie at depths between 1450 m and 2450 m below the surface and the whole detector has a volume of $\sim 1\,\mathrm{km}^2$, allowing for detection of neutrinos at energies above 100 GeV.

Event types IceCube observes Cherenkov light produced by charged particles created in interactions between neutrinos and ice. There are three main signatures of neutrino events: "track-like", "shower-" or "cascade-like" and "double-bang" events. "Track-like" events are the most suitable for the detection of potential point-like astrophysical sources. They are mainly generated by muons produced in charged-current (CC) weak interactions of muon neutrinos: $\nu_\mu + N \to \mu + X$, where N is a nucleon and X a hadronic shower. Muons lose energy by radiative emission above 700 GeV, constantly producing light all along the track. At TeV energies and in the Antarctic ice, the muon path length reaches several kilometers, allowing for an increased event rate (neutrino interactions happening far ouside the instrumented volume can still be detected) and improved particle tracking (angular resolution $< 1°$), albeit with a bad energy resolution, since an indefinite amount of energy could be deposited outside the instrumented volume. Despite such good angular resolution and the fact that the transparency of deep Antarctic ice improves detection efficiency, the event reconstruction is made difficult by photon scattering and the complexity of the optical properties of the ice, which change with depth and are altered around the DOMs.

Background A good track reconstruction has a fundamental importance in background rejection. Most signals are indeed due to background muons and neutrinos produced in cosmic-ray air showers: only about one in a million events comes from a neutrino interaction, but the sample is actually large enough ($\sim 10^5 \text{year}^{-1}$) to allow for a good characterization of the high-energy neutrino spectrum and spatial distribution. Two event types are taken into consideration when discriminating "good" track-like events from cosmic-ray background: *starting* and *through-going* tracks. Through-going tracks are produced by muons crossing the detector after being generated by neutrino interactions outside the instrumented volume. A natural filter is employed to select the right events: the Earth. Cosmic-ray muons from the northern hemisphere cannot cross large rock depths and interact with IceCube before being absorbed. Therefore, *up-going* (zenith angle $\gtrsim 85°$) muons could only originate from neutrino interactions. Residual false positives with poorly reconstructed tracks are discarded through statistical techniques which evaluate track reconstruction quality with the decision tree method. Particles from the southern sky, however, are not ignored altogether: spurious signals are recognized by the vetoing action of IceTop and the evaluation of some additional event parameters, which imposes a higher energy threshold (over ~ 100 TeV). Down-going tracks are actually privileged when looking for starting tracks, whose interaction vertex is searched for inside the detector to increase signal purity at the expense of event rate and angular resolution.

Results As already said, the result is still dominated by neutrino-induced events of atmospheric origin. Models and Monte Carlo simulations of the atmospheric spectra are well fitted by experimental data at low energies [23]. The spectra are consistent with simple power laws with high indices ($\sim E^{-3.7} - E^{-4.0}$ for the *conventional* component due to muon neutrinos produced in pion and kaon decay; see [3]). Their steep decrease allows to recognize the *cosmic* excess flux at high energies. It has been found that suspect cosmic signals are incompatible with the atmospheric origin hypothesis at above 4σ. The cosmic neutrino spectrum is consistent with an unbroken power law with a spectral index of -2.13 ± 0.13 above 200 TeV. The spatial distribution looks isotropic, thus suggesting that a large fraction of the flux has an extragalactic origin.

Before the IceCube-170922A event, no positive detections of individual neutrino sources had been made ([4], [23], [3]). A maximum likelihood technique is used to estimate the plausibility of a localized excess over the diffuse background, and the found p-values are

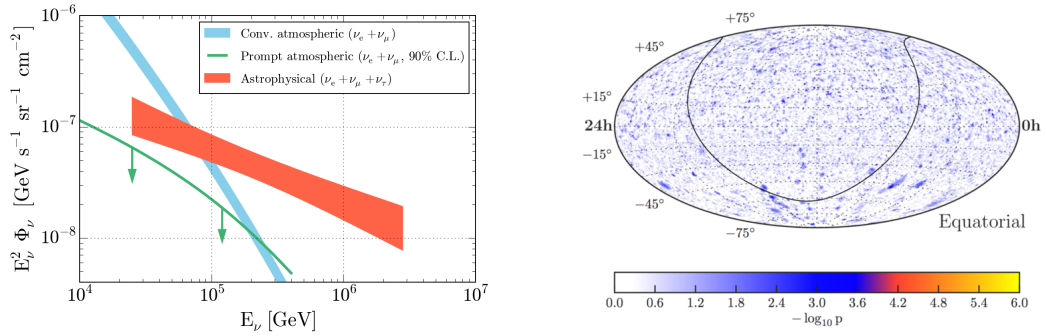

(a) (b)

Figure 2.3: (a): best-fit neutrino spectra assuming a single power-law model. The blue and red areas correspond to the 68% C.L.. See [2]. (b): all-sky pre-trial likelihood map of neutrino clustering due to potential point sources, computed with 7 years of IceCube data. See [3]

compared to randomly generated ones to estimate their significance. Both this line of research and focused analysis of known gamma-ray sources and transients found results compatible with background fluctuations. The diffuse neutrino emission was thus been interpreted as originating from a large number of individual unresolved sources, and lower limits on the presumed contributions of various source populations were computed[2]. A study [4] found that the contribution of 2LAC (Second Fermi LAT AGN Catalog) blazars is around 25%, but falls at below 10% if a strict proportionality is assumed between the emitted power in gamma rays at GeV energies and in neutrinos at TeV energies.

2.4 IceCube-170922A

In order to improve the outcome of these source identification attempts, the IceCube collaboration has been releasing real-time alerts of astrophysical neutrino detections since April 2016 through the GCN/TAN. This allows follow-up observation campaigns by the other instruments in the network, to validate the events and study them with a comprehensive, multimessenger approach based on data taken almost immediately.

The tenth such notice was released on September 22, 2017 at 20:55:13 UTC, 43 seconds after the detection of a high-energy neutrino-induced muon track event at 20:54:30.43 [16]. The notice was the result of a first automated data processing which obtained a preliminary estimate of the direction and energy of the event. About 4 hours later, a GCN Circular [22] communicated improved results, which were further refined by subsequent analysis and compared with data from the other observatories in the network.

2.4.1 IceCube analysis

Track reconstruction and position estimate

The final best fit result for the candidate source position is $RA = 77.43^{+0.95}_{-0.65}$, $Dec = +5.72^{+0.50}_{-0.30}$ (deg, J2000, 90% containment region). The equatorial position of the candidate source (cos(zenith) $= -0.1$) falls in the most sensitive acceptance range, where atmospheric

[2]Recent studies [19] suggest instead a correlation between the spectrum of astrophysical neutrinos above 100 TeV and the diffuse component of the EGB measured by Fermi.

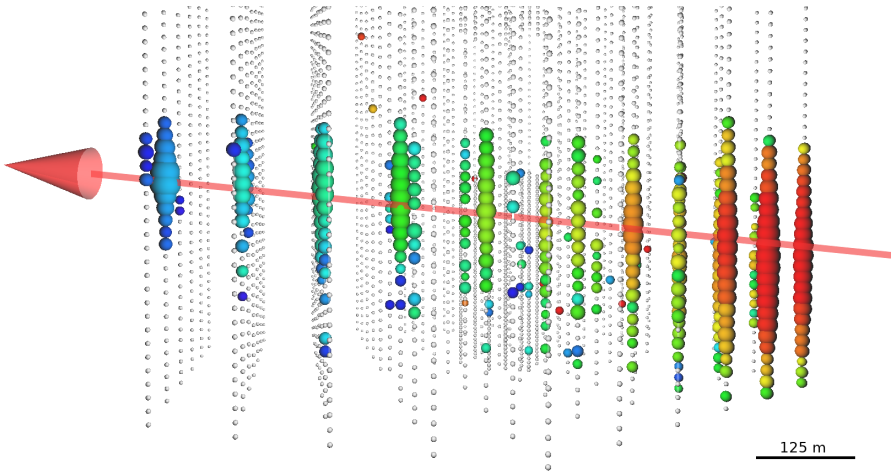

Figure 2.4: Event display for neutrino IceCube-170922A. The arrow shows the best-fit track direction. The size of the spheres is proportional to the logarithm of the amount of light collected at each DOM. The colours match the observation time of the signal (red = earliest hits, blue = latest hits) [24].

muons are mostly blocked, but the Earth does not absorb a large fraction of the neutrino flux. The tracks were reconstructed using a log-likelihood fit which compared the experimental DOM response with the expected response, obtained by modeling the propagation of Cherenkov photons. The expected uncertainties were thus computed by simulating a large number of similar events (tracks closer than 30 m and directions within 2° of the best-fit result, total deposited charge within ±20% of the measured value of ∼ 5800 photoelectrons) and finding, for each one, the value of the test statistic $TS = 2(\log \mathcal{L}_{\mathrm{MC}} - \log \mathcal{L}_{\mathrm{best}})$. Confidence regions were then extracted from the TS distribution. This allowed to take into account the average systematic error due to imperfect modeling of the optical properties of the polar ice.

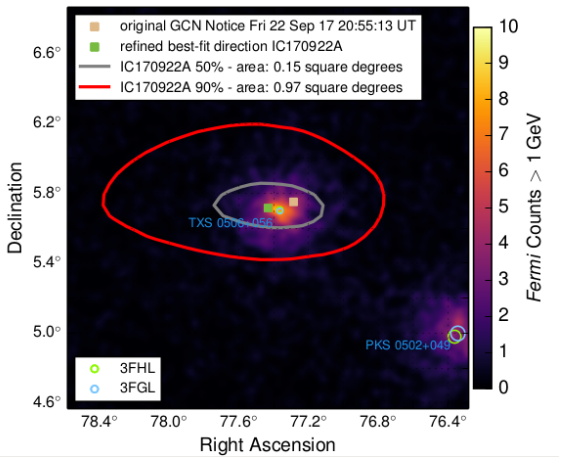

Figure 2.5: Sky position of IceCube-170922A overlaying the gamma-ray photon counts from the Fermi LAT above 1 GeV [24].

Energy reconstruction

22 TeV of energy were deposited inside the detector but, since the event was a through-going track, an indirect estimate of the neutrino energy was made by simulating the detector response. Energy losses for muons above 1 TeV, mainly due to Bremsstrahlung, pair production and photo-nuclear interactions, grow with muon energy. This relation and the corresponding probability density functions of neutrino energy, obtained from simulations, allow to reconstruct the true energy of the primary particle from the *truncated energy* deposited in the detector. If the measured spectral density of $\frac{dN}{dE} \propto E^{-2.13\pm0.13}$ for the diffuse muon neutrino background is chosen, the IceCube-170922A true energy is estimated at 290 TeV, with a 90% C.L. lower limit of 183 TeV.

2.4.2 Multiwavelength follow-up observations

The muon neutrino spectrum and the simulations have also been used to compute the so-called "signalness" of the event, the probability that the recorded track actually came from an astrophysical neutrino interaction and not from a cosmic-ray air shower. It has been estimated at about 50%, thus an atmospheric origin cannot be totally excluded: robust identifications with astrophysical neutrinos are possible only at PeV energies. Consequently, multiwavelength observations of the electromagnetic emission in the immediate aftermath of the event can be critical. The ANTARES neutrino telescope was alerted too, but did not detect any signal from the candidate source region.

High-energy gamma rays

On September 28, 2017, the Fermi LAT Collaboration announced [39] that a known high-energy gamma-ray source had been found inside the IceCube-170922A error region, 0.1° from the best-fit neutrino direction. The BL Lac blazar TXS 0506+056[3] was being monitored as a flaring object by both the Automated Science Processing (ASP) and the Fermi All-sky Variability Analysis (FAVA). ASP finds clusters of photons in LAT data in different time intervals (6 hours, 1 day, 1 week) and energy ranges. FAVA performs blind searches of flares and transients: it looks for flux variations with respect to the first four-year average on a weekly time scale and on two energy bands using a photometric approach, which is independent from the diffuse gamma-ray background model, and then refines the result with a maximum likelihood analysis when the deviation exceeds 4σ significance. FAVA found a photon flux excess with 6.5σ significance (likelihood analysis) in the low-energy band (0.1 GeV to 0.8 GeV) and 6.9σ significance in the high-energy band (0.8 GeV to 300 GeV) in the neutrino detection time bin (527442218-528047018 MET[4]). A brightness increase in the GeV band starting from April 2017 was also observed by FAVA. Two light curves were computed using Fermi LAT Pass 8 data in the energy range above 0.1 GeV: one from August 4, 2008 to October 24, 2017 with 28-day-long time bins, and another one for a shorter time period around the neutrino detection, with 7-days-long time intervals. The curves were obtained with the maximum likelihood technique, binned in space and energy, over a $10° \times 10°$ region of interest around the source position as listed in the 3FGL catalog. The whole calculation was performed taking into account all the sources in the region of

[3] Texas Survey of Radio Sources nomenclature. The same object is listed as J0509.4+0541 in the Third Fermi-LAT Source Catalog (3FGL) and as J0509.4+0542 in the Third Catalog of Hard Fermi-LAT Sources (3FHL).

[4] The Mission Elapsed Time (MET) is the number of seconds since the reference time of January 1, 2001 at 00:00:00 UTC, corresponding to a Modified Julian Date (MJD) of 51910 in the UTC system.

interest, the diffuse background, and some additional weak candidate sources. The highest flux ($(5.3 \pm 0.6) \times 10^{-7}\mathrm{cm}^{-2}\mathrm{s}^{-1}$, about 7 times the integrated flux averaged over all Fermi LAT observations) was observed between July 4 and July 11, 2017, while the most noticeable variation during the flare was seen between August 8 and August 22.

Fermi LAT results have been corroborated by the observations made with the Italian satellite AGILE between September 10 and September 23.

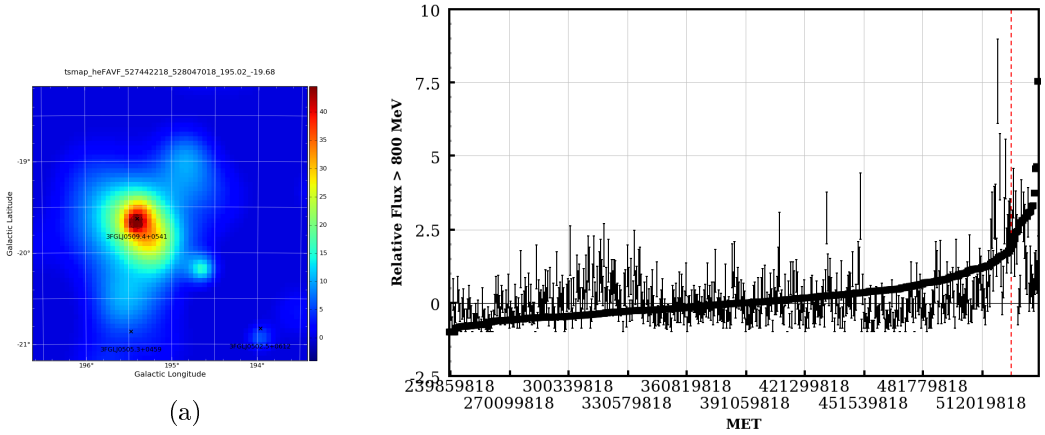

(a) (b)

Figure 2.6: FAVA results for TXS 0506+056 at high energies (800 MeV − 300 GeV). (a): TS map in the neutrino alert time bin. (b): light curve between August 2008 and March 2018 [28].

Very-high-energy gamma rays

Starting from few hours after the neutrino alert, many ground-based Imaging Atmospheric Cherenkov Telescopes performed observations of the TXS 0506+056 region in the TeV gamma-ray band. Neither H.E.S.S. nor VERITAS detected gamma-ray emission from the source, thus putting upper limits on the photon flux at $E > 175\,\mathrm{GeV}$. Another null outcome above 1 TeV was obtained by the HAWC observatory. The MAGIC telescopes initially did not detect anything either during their first observation session on September 24. A second observation sequence between September 28 and October 4, prompted by the Fermi LAT announcement, found a 6σ excess over the expected background at energies up to 400 GeV. This may represent the first detection ever of very-high-energy gamma rays consistent with an astrophysical neutrino event.

Other wavelengths

Radio observations by the Karl G. Jansky Very Large Array (VLA) and the OVRO found significant flux variability of the candidate source in the months preceding the event and the weeks following it. Optical observatories (ASAS-SN, Liverpool, Kanata, Kiso, SALT, Subaru, VLT) measured an increased flux in the V band and a spectral energy distribution shift towards shorter wavelengths. Among X-ray instruments, only the Neil Gehrels Swift Observatory and NuSTAR yielded interesting outcomes, while MAXI and INTEGRAL returned null results: the two NASA space telescopes observed increased variability and flux and measured spectra which well connect to the Fermi ones. All these data match the typical behaviour of blazar flares.

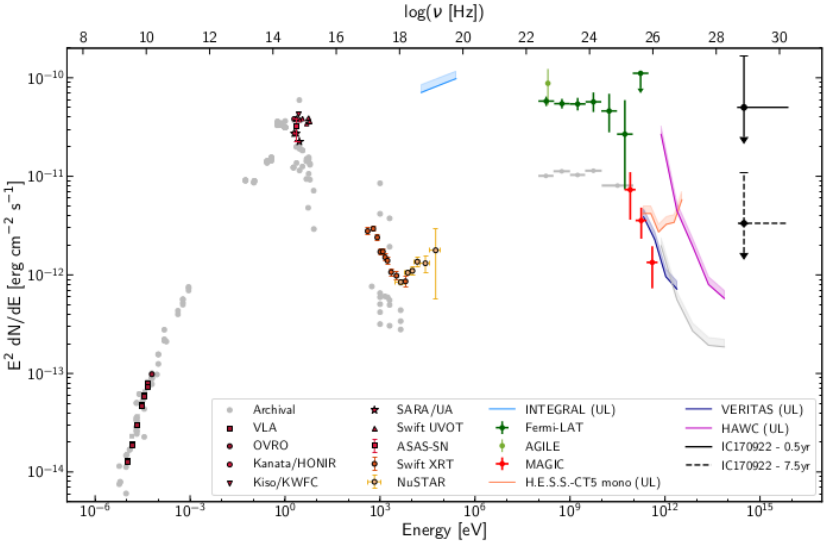

Figure 2.7: Broadband Spectral Energy Distribution of TXS 0506+056 based on observations performed in the first 14 days after the IceCube-170922A neutrino detection [24].

2.4.3 Chance coincidence probability

Such a tight positional coincidence between the reconstructed direction of an astrophysical neutrino and a known high-energy photon source is unprecedented, and can be used to estimate the probability that it actually reflects a common physical origin (a blazar flare in particular) for the two kinds of particles rather than a mere chance. It has been demonstrated that the energy output of some blazars is high enough to explain some IceCube detections [29], while [4] showed that most of the blazar contribution to IceCube neutrino observations should be constrained to the quasi-diffuse background; very few associations with single sources during the entire lifetime of the instrument are however still compatible with this conclusion, so every single event can be critical. The p-values of various correlation scenarios are computed *a posteriori* by simulating neutrino events (including atmospheric neutrinos and misidentified muons) and building light curves for 2257 extragalactic Fermi LAT sources listed in the 3FGL and 3FHL catalogs. No *a priori* assumption on neutrino - blazar correlation was made before the event because neutrino production mechanisms could be diverse and are still poorly understood; some correlation models are instead evaluated after the observation using a log-likelihood ratio test statistic similar to the one employed for source identification (for example, see [3]):

$$TS = 2\log\frac{\mathcal{L}(n_s = 1)}{\mathcal{L}(n_s = 0)} \tag{2.7}$$

where

$$\mathcal{L} = \prod_i^N \left(\frac{n_s}{N}\mathcal{S} + (1 - \frac{n_s}{N})\mathcal{B}\right) \tag{2.8}$$

and n_s is the number of signal events, N the total number of events, $\mathcal{S}$ and $\mathcal{B}$ are the probability distribution functions of the signal and the background respectively. Therefore $TS = 2\log\frac{\mathcal{S}}{\mathcal{B}}$ in this case. $\mathcal{S}(\vec{x}, t)$ consists of three independent factors: the spatial weight, that models the IceCube PSF accounting for the distance between the gamma-ray source and the neutrino direction in terms of the neutrino angular uncertainty; a flux weight describing the relation between gamma-ray flux and expected neutrino flux; and an IceCube

acceptance factor linked to the zenith distribution of the alerts due to background. The p-values are then computed as the fraction of background TS values larger than the measured one for IceCube-170922A. Three joint neutrino and gamma-ray production models are tested:

1. Pion decay from pp or $p\gamma$ interactions dominates, so the neutrino energy flux is proportional to the gamma-ray energy flux in the time bin where the neutrino arrives;
2. The neutrino production and detection probabilities depend only on the relative gamma-ray flux change (temporal correlation), so that even weak gamma-ray sources can be considered;
3. The neutrino flux is proportional to the VHE gamma-ray flux, which should be detected from objects able to accelerate hadrons up to PeV energies.

Other tests are performed separately to evaluate the impact of the spatial factor. The global p-value is then found by applying a trial factor correction to account for the IceCube detection of 50 other alert-worthy neutrino events before September 22, 2017: $p_{\rm global} = 1-(1-p_{\rm local})^N \approx p_{\rm local}N$, $N = 51$; $p_{\rm global} = 3.0\sigma$ for models 1 and 2, $p_{\rm global} = 3.6\sigma - 2.8\sigma$ for model 3, depending on N (not all alerts trigger VHE observations). This means that chance coincidence of IceCube-170922A with the flare of TXS 0506+056 is disfavoured at about 3σ level. The validity of hadronic hypotheses on neutrino and gamma-ray photon production is supported also by this argument on the source luminosity: since the muon neutrino fluence needed to expect an event similar to IceCube-170922A in the full time period starting from May 2010 is 2.8×10^{-3} erg cm^{-2}, assuming a spectrum with an index of -2 and the redshift of $z = 0.38 - 0.98$ obtained from multiwavelength data, a neutrino isotropic luminosity of $\sim 10^{47}$ erg s^{-1} is estimated, which is similar to the observed gamma-ray isotropic luminosity of TXS 0506+056. On the other hand, simulations of neutrino signals following model 1 show that in 14% of the cases a neutrino would be detected in coincidence with a source as bright as TXS 0506+056 or more. This proves that a single neutrino observation is indeed not enough to confirm or reject the neutrino - blazar connection, nor to support or confute a certain production model. More detailed studies are needed and new observations are desirable; a short preliminary analysis for future work is presented in the next chapter.

Chapter 3

Data Analysis

3.1 Variability studies with Fermi LAT data

Transient and variable sources are studied with a variety of approaches besides the already-mentioned FAVA. Source catalogs like 3FGL provide monthly light curves and variability indices based on the maximum likelihood method. Preliminary data (*e.g.* daily and weekly light curves) on a number of sources exceeding $1 \times 10^{-6}\,\mathrm{cm}^{-2}\mathrm{s}^{-1}$ flux are provided by the Monitored Source List[1], while shorter-term variability analysis of flaring objects is performed and communicated by the Fermi-LAT Flare Advocate/Gamma-ray Sky Watcher program[2].

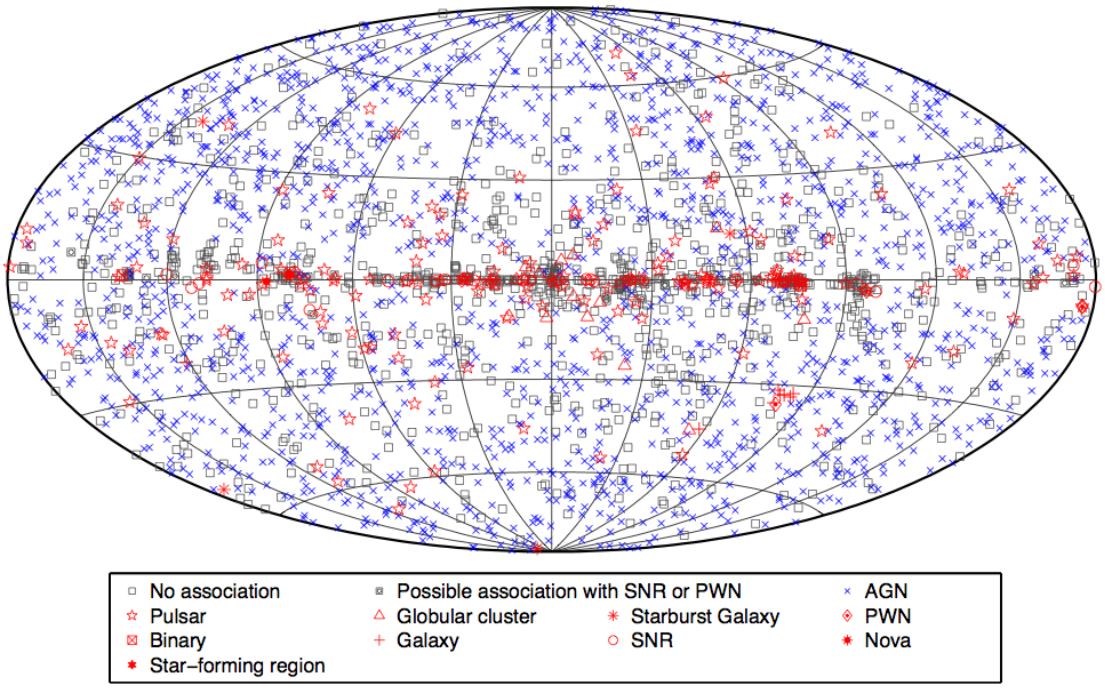

Figure 3.1: The 3FGL Catalog [13]. Galactic coordinates, Hammer-Aitoff projection.

[1] See `https://fermi.gsfc.nasa.gov/ssc/data/access/lat/msl_lc/`
[2] See `http://fermisky.blogspot.com/`

3.1.1 3FGL and Variability

The third Fermi Large Area Telescope source catalog (3FGL) was published in 2015 and lists high-energy gamma-ray sources detected in the first four years of observations. It features 3033 sources[3] above 4σ significance. Information on sources, from detection and localization to the spectral representation, fluxes and variability, is obtained and provided by the use of test statistics $TS = -2(\log \mathcal{H}(\text{null}) - \log \mathcal{H}(\text{alternate}))$ and their comparison with some threshold values matching certain confidence levels. The alternate hypothesis refers to the scenario where fluxes, etc. get the optimal (maximum-likelihood) values obtained from an iterative fit procedure over spatial, time or energy bins.

Light curves and variability The significances of detection, localization, curvature and flux are computed on the whole four-year period, so the catalog does not feature transients, nor highly variable sources that average below the detection threshold ($TS = 25$) during the four-year period (which is the main reason behind the "disappearance" of some sources already included in 2FGL). It deals, however, with source variability for objects meeting the insertion criteria. The observation period is divided into 30.37 days long time intervals. The length of these bins preserves some statistical precision on the faint sources and minimizes systematic errors associated with the orbit precession period (27.6 days). All the spectral shape parameters are frozen to avoid large error bars: spectral indices are kept fixed to the values obtained in the full interval (it is expected that changes in the spectral shape would induce a change in photon fluxes anyway), so are the spectral parameters of the Galactic diffuse background. The gamma-ray background model also takes into account the emission from the Earth limb, the Moon and the Sun (including solar flares). Fluxes are then obtained by optimization in each bin with the log-likelihood procedure, using unbinned likelihood over the full energy range[4]. For sources with $1 < TS < 10$ best-fit flux values F_i are retained instead of using 2σ upper limits, but upper and lower errors are computed with the so-called *profile* method (an upper limit is found when $2\Delta \log \mathcal{L} = 4$ when increasing the flux from the maximum likelihood value). If $TS < 1$, a *Bayesian* method ($\mathcal{L}(F_i)$ is integrated from 0 up to the flux encompassing the 95% posterior probability) is preferred and upper limits are indicated. The Bayesian approach is only used in this special case because fluxes and upper limits are about five times longer to compute; this makes an accurate selection of variable sources even more important to optimize the computational cost as much as possible.

Variability is then tested with the introduction of a *variability index*:

$$TS_{\text{var}} = 2[\log \mathcal{L}(\{F_i\}) - \log \mathcal{L}(F_{\text{const}})] = 2 \sum_i [\log \mathcal{L}_i(F_i) - \log \mathcal{L}_i(F_{\text{const}})] = 2 \sum_i V_i^2 \quad (3.1)$$

where $\log \mathcal{L}(\{F_i\})$ is the log-likelihood for the alternate hypothesis, in which the flux is optimized for each individual time interval. F_{const} is the flux when it is presumed constant over the whole four-year observation period (null hypothesis). Its value is close, but not always equal (especially when there are strongly variable sources in the background), to the maximum likelihood best fit over the full time period. For sources of low significance, upper limits are always estimated with the profile method, even when $TS < 1$. To account for systematic errors due to the dependence of the Instrument Response Functions on the

[3] The number of entries is 3034, but the Crab PWN is represented as *two* co-spatial sources to account for the complexity of its spectrum.

[4] The best-fit overall fluxes are instead computed over the full observation period, but dividing the energy range into five bins.

viewing angle, the terms of the sum are scaled, so that the variability index is in fact this:

$$TS_{\text{var}} = 2\sum_i \frac{\Delta F_i^2}{\Delta F_i^2 + f^2 F_{\text{const}}^2} V_i^2 \tag{3.2}$$

$f = 0.02 = 2\%$ is a correction factor measured on the fluxes from bright pulsars. Like the previous test statistics, the variability index does not tell how much a source is variable, but only checks the plausibility of the alternate hypothesis with respect to the null hypothesis (the source being constant). Moreover, it addresses only variability on a scale of months, and is less sensitive to longer- or shorter-term variations. The index follows a χ^2 distribution with 47 degrees of freedom (48 time bins minus the constraint put by F_{const}, which is not known *a priori*). A source is therefore considered variable at the 99% confidence level when $TS_{\text{var}} > 72.44$.

3.2 Finding variable sources in 3FGL

The three models for the joint neutrino and gamma-ray production and detection considered in the IceCube-170922A likelihood analysis (see Section 2.4.3) define relationships between neutrino and gamma-ray flux or variability. Assuming that a fraction of gamma rays are produced in a hadronic scenario, the probability that neutrinos are produced increases during flares, when the gamma-ray flux is much higher than during quiescent phases, and the more a source is prone to flaring (*i.e.*, it is variable) the higher it is likely to emit detectable neutrinos. Consequently, assessing the probability that a cosmic neutrino is correlated to an AGN flare, thus confirming the hadronic scenario, needs a careful study of the variable extragalactic gamma-ray source population. Highly variable objects in 3FGL often do not show enough significance in all the time bins, so building light curves involves using variable bins and the computation of upper limits and errors with the profile or Bayesian methods which, as already said, are much longer and more expensive from a computational point of view. Selecting only the most variable sources for the study thus allows to estimate in advance how much resources and time are needed.

3.2.1 Data selection

The variability threshold as defined before comes from the probability density function followed by variability indices for every single source (the event space is all the variability indices of the same source computed from an infinite sample of 48-month time periods). The approach used here instead tries to find a threshold value of the variability index to pinpoint the *most variable* objects among the extragalactic gamma-ray sources, by analyzing the empirical frequency density of variability indices.

First, 3FGL sources have been filtered according to their class designation (CLASS1 column of the FITS file). Only extragalactic and unassociated sources have been selected for the analysis. As already explained, AGNs are among the "prime suspects" of the high-energy gamma ray - astrophysical neutrino correlation at high Galactic latitudes. Galactic objects generally show variability at lower confidence levels (see Figures 3.4 and 3.5) and they are thought to contribute mainly to the diffuse neutrino background as unresolved sources [23], so they have been ignored in this work. Non-active galaxies and unassociated objects are kept in the sample to avoid discarding potential extragalactic neutrino sources (see Figure 3.6). The selected entries are:

Source class	Number of entries
Unassociated	1010
Compact Steep Spectrum Quasar (CSS/css)	1
BL Lac type of blazar (BLL/bll)	660
FSRQ type of blazar (FSRQ/fsrq)	484
Non-blazar active galaxy (AGN/agn)	3
Radio galaxy (RDG/rdg)	15
Seyfert galaxy (SEY/sey)	1
Blazar candidate of uncertain type (BCU/bcu)	573
Normal galaxy (or part) (GAL/gal)	3
Starburst galaxy (SBG/sbg)	4
Narrow line Seyfert 1 (NLSY1/nlsy1)	5
Soft spectrum radio quasar (SSRQ/ssrq)	3
Total	2762

Table 3.1: Selected sources from the 3FGL catalog.

3.2.2 Empirical distribution

The variability index interval (from 2.29×10^{01} to 6.07×10^{04}) of the selected sources has then been subdivided into bins to build a frequency density histogram. The Freedman-Diaconis rule has been chosen as a good compromise between the need to limit the number of bins to a resonable value and to avoid oversmoothing: $W = 2\frac{IQR}{N^{\frac{1}{3}}}$ where $W = 3.78$ is the bin width, $IQR = 26.51$ is the interquartile range of the sample and $N = 2762$ is the number of entries. The number of bins thus obtained (16068) has been reduced to 60 after merging some of them in order to get at least 5-10 entries per interval and therefore compute Poisson errors on the bin height:

$$h_i = \frac{n_i}{w_i} \tag{3.3}$$

where h_i is the $i-$th bin height, n_i the number of entries in that bin, and w_i the bin width;

$$\sigma_{h_i} = \frac{\sigma_{n_i}}{w_i} = \frac{\sqrt{n_i}}{w_i} \tag{3.4}$$

Figure 3.2 is the resulting histogram with logarithmic scale on the x axis. The presumed source of the IceCube-170922A neutrino event, blazar TXS 0506+056, has a variability index of 2.85×10^{02}, meaning that it is a variable object at over the 99% C.L.: see figure 3.3.

3.2.3 Source populations

Using the same variability index bins allows to show visually why Galactic sources have been ignored in this analysis. See Figure 3.4 for the frequency density histogram of the variability indices of Galactic sources, and Figure 3.5 for a comparison with the histogram relative to all the other sources in 3FGL. While some of these objects even have a steady flux at the 100% C.L. ($TS_{\text{var}} = 0$) on a monthly timescale, the majority of Galactic sources show a limited confidence on variability, with only 21 entries (7.7%) exceeding the 99% threshold of $TS_{\text{var}} = 72.44$. This suggests that most Galactic objects are indeed steady gamma-ray sources, so that their light curves can be computed using simple fixed-width time bins. The fraction of high-confidence variable objects is higher among extragalactic-plus-unassociated sources (626 objects, or 22.7%) and highest among the extragalactic

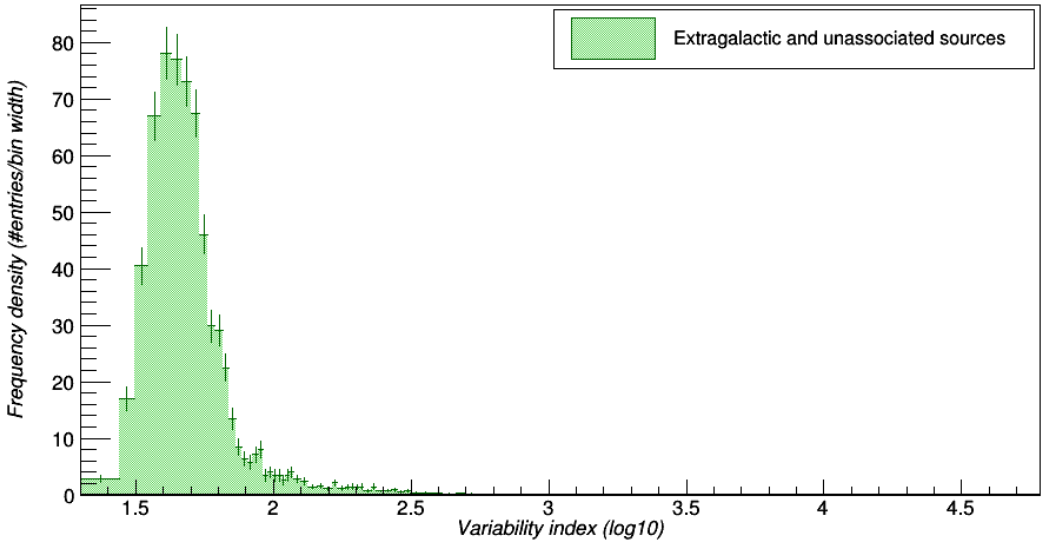

Figure 3.2: Frequency density histogram of the variability indices of extragalactic and unassociated sources in 3FGL (logarithmic scale).

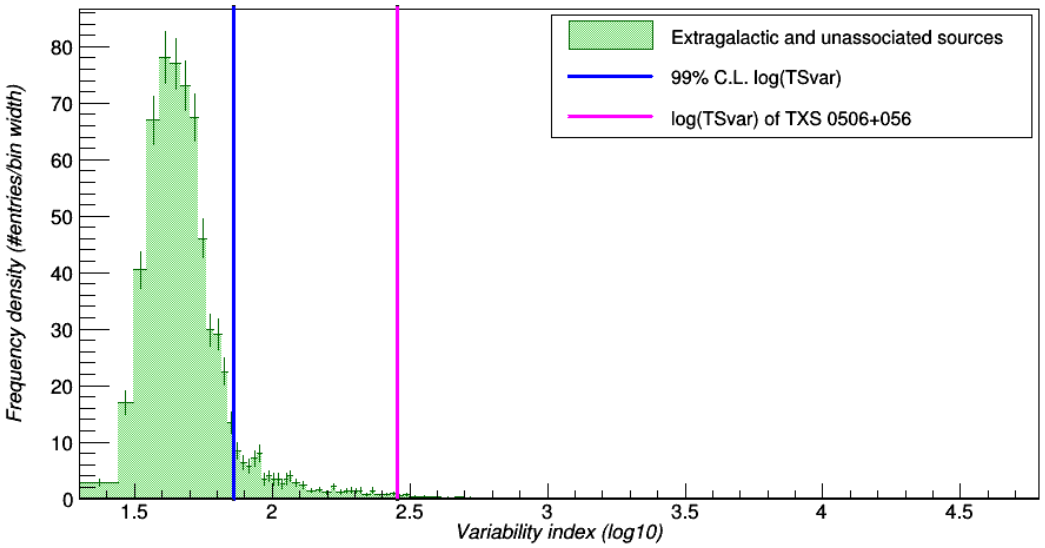

Figure 3.3: Frequency density histogram of the variability indices of extragalactic and unassociated sources in 3FGL (logarithmic scale) with the position of the 99% C.L. threshold on variability and of the blazar TXS 0506+056 variability index.

sources only (600 objects, or 34.2%), while it is very low among the unassociated sources only (26 objects, or 2.6%). The histograms in Figure 3.6 show the frequency densities of variability indices of extragalactic and unassociated sources separately. It is evident from the lack of a long "tail" at high variability indices that detecting variability with a high confidence level in unassociated sources is more difficult, mainly because of the large fraction of Galactic objects belonging to this category: see Figure 3.7. It is worth mentioning that a large fraction of them (40%) has at least one "analysis flag" set in the catalog to remind that some information in these cases is not as significant as data on other sources [9]. Many of the unassociated sources lie near the Milky Way plane (Galactic latitude $|b| < 5°$). Extrapolating the object density values in the regions ouside the plane

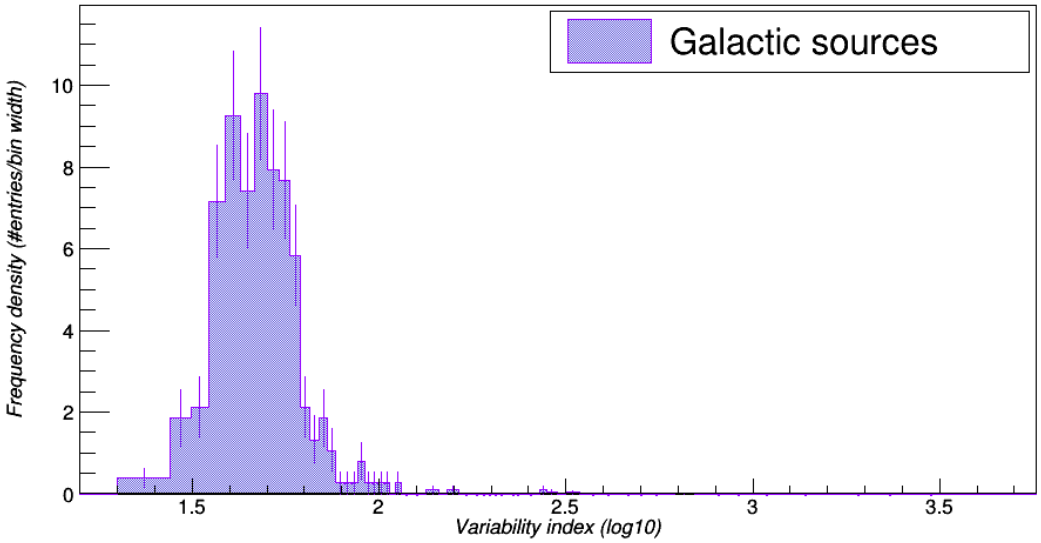

Figure 3.4: Frequency density histogram of the variability indices of Galactic sources in 3FGL (logarithmic scale).

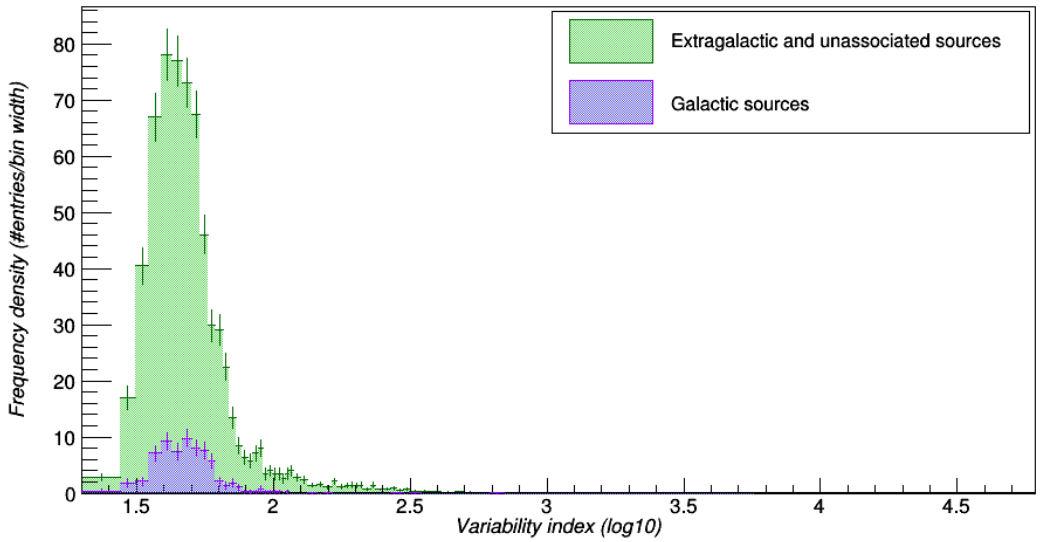

Figure 3.5: Comparison between the frequency density histograms of the variability indices of Galactic sources and all the other objects in 3FGL (logarithmic scale).

and the population counts known from associated and identified objects, it is estimated that around 160 AGNs should be observable at low latitudes; 56 of them are known, so around 100 unassociated sources or less in the Milky Way plane could be active galaxies. The other ~ 235 ($\sim 23\%$ of unassociated objects), then, should be Galactic sources, mainly pulsars and supernova remnants. Most of unassociated objects lie far from the Galactic plane ($|b| > 5°$) anyway, and thus are extragalactic sources which may be useful for future analysis as potential neutrino-producing AGNs.

3.2.4 Tentative histogram fitting

At this point, several attempts have been made to fit the frequency density histogram for unassociated and extragalactic sources with a known function, or a sum of known functions.

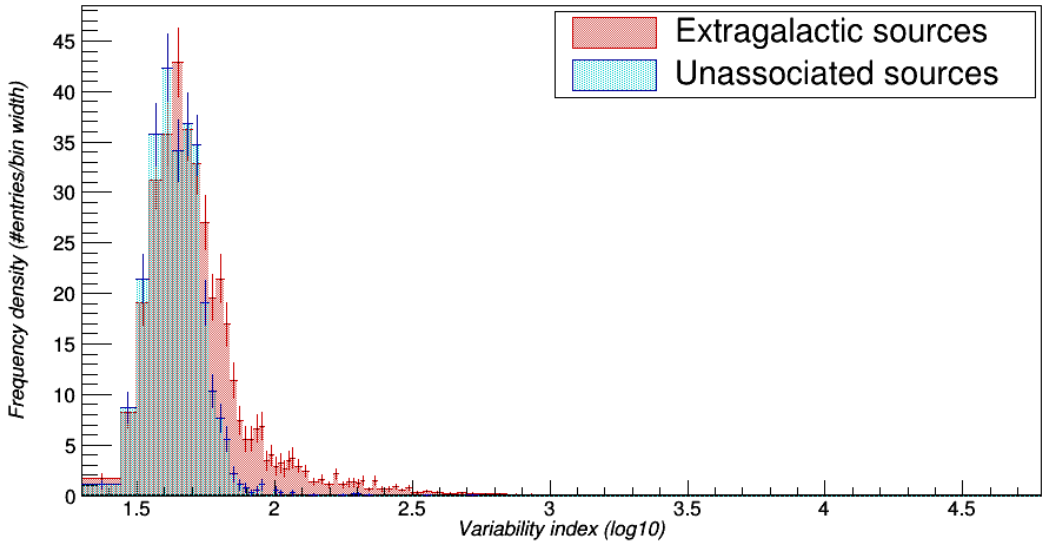

Figure 3.6: Comparison between the frequency density histograms of the variability indices of extragalactic sources and unassociated sources in 3FGL (logarithmic scale).

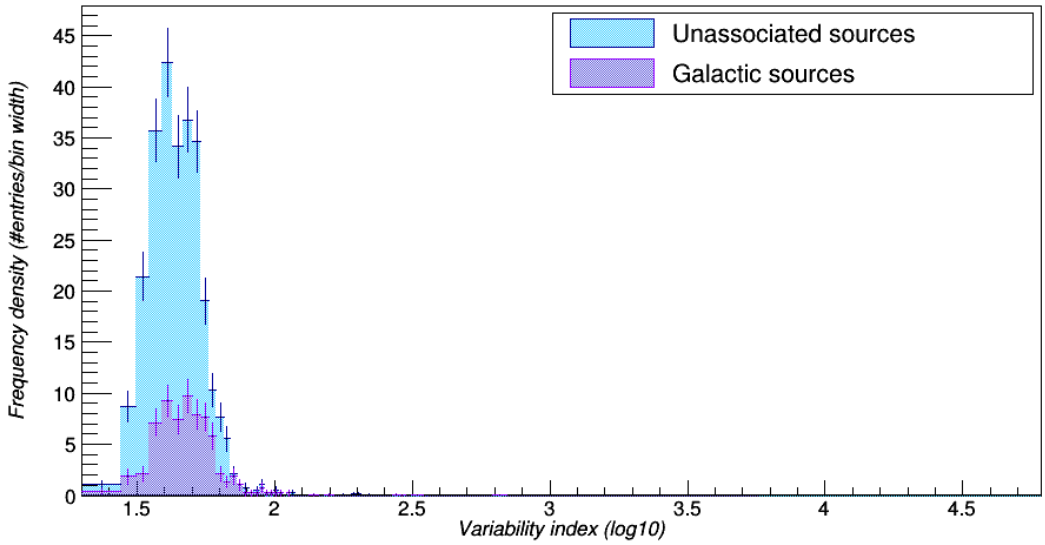

Figure 3.7: Comparison between the frequency density histograms of the variability indices of Galactic sources and unassociated sources in 3FGL (logarithmic scale).

All the fits have been performed using ROOT 6.12/06.

The best results have been obtained with sums of two functions: normal or skew-normal distributions. The choice of these functions is totally empirical and does not bear any physical meaning for now. None of the attempts has yielded a satisfying outcome, the reduced chi square (~ 2) or the residuals being too high, or the graph showing overfitting of some bins. In case of a good fit, the threshold $\log(TS_{\text{var}})$ would have been at the intersection of the two final fit functions.

Best attempt: two skew-normal functions The histogram has been fitted by a sum of two skew-normal distributions on the whole interval of $\log(TS_{\text{var}})$ from 1.30 to 4.80. To inizialize the parameters before the overall fit, a first skew-normal function has been fitted

on the interval from 1.30 to 1.90 and a second one on the interval from 1.85 to 4.80. The procedure has been performed on the basis of the integral value, using the χ^2 method for a weighted fit.

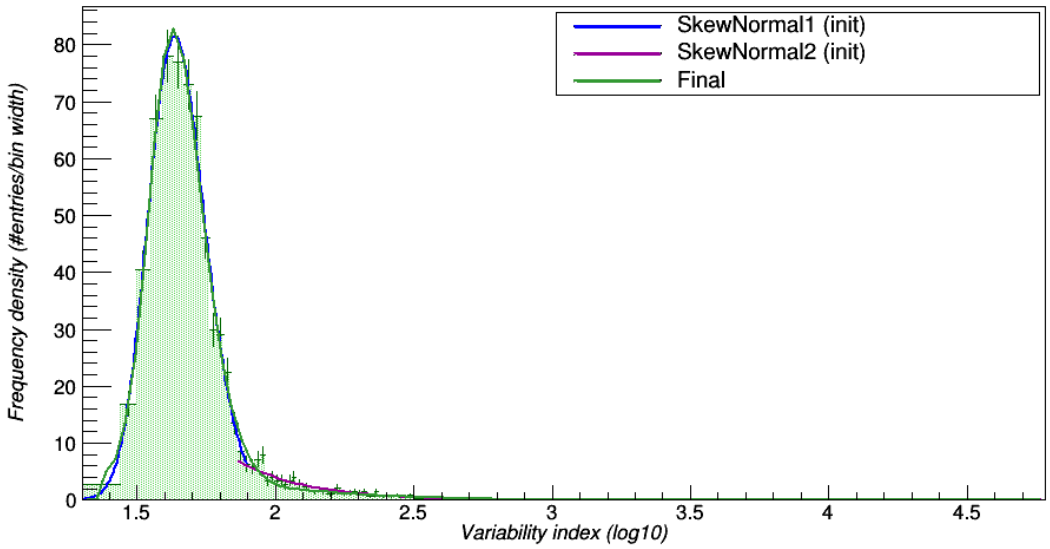

Figure 3.8: Graphs of the fitting function (sum of two skew-normal functions) and of the two initialization functions (truncated skew-normal) above the density frequency histogram of extragalactic and unassociated sources in 3FGL.

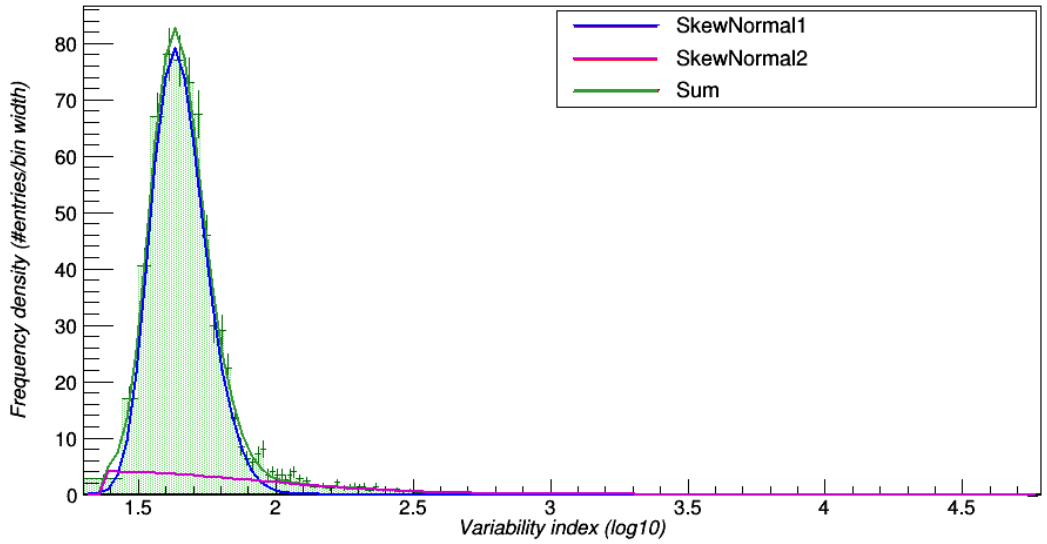

Figure 3.9: Graphs of the fitting function and of its two addends taken individually.

$$f(x) = \frac{p_0}{p_2\sqrt{2\pi}} \mathrm{e}^{-\frac{1}{2}\left(\frac{x-p_1}{p_2}\right)^2} \operatorname{erfc}\left(-\frac{p_3(x-p_1)}{p_2\sqrt{2}}\right) + \frac{p_4}{p_6\sqrt{2\pi}} \mathrm{e}^{-\frac{1}{2}\left(\frac{x-p_5}{p_6}\right)^2} \operatorname{erfc}\left(-\frac{p_7(x-p_5)}{p_6\sqrt{2}}\right) \tag{3.5}$$

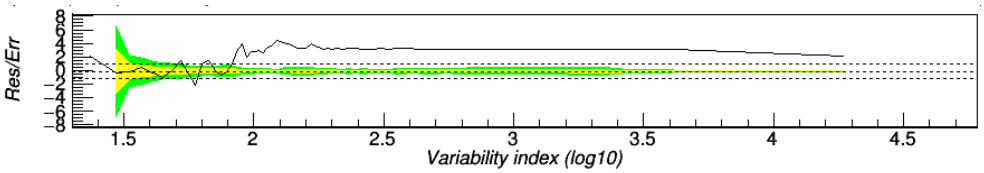

Figure 3.10: Plot of the residuals divided by the statistical uncertainty from the histogram. The green and yellow areas show the 1σ and 2σ confidence intervals, respectively.

Parameter	Value	Parabolic error
p_0	19.4	0.5
p_1	1.555	0.007
p_2	0.140	0.006
p_3	1.8	0.3
p_4	2.8	0.3
p_5	1.38	0.02
p_6	0.56	0.02
p_7	234	1
χ^2/ndf[a]	71.92/52=1.38	

[a] Number of degrees of freedom

Table 3.2: Histogram fit parameters

Conclusions

This work has outlined a method to select variable high-energy gamma-ray objects to study as potential neutrino sources by fitting the empirical density frequency histogram of variability indices of 3FGL sources to a known function, and then computing a reasonable threshold value, on the basis of the function integral, to discriminate the sources with the highest variability confidence in the sample. This allows to optimize the quantity of data to process, and thus the computational cost, to build the light curves needed to estimate the probability that neutrinos detected by IceCube are produced in hadronic processes in active galactic nuclei. Those histograms will soon be updated by taking into account all the sources belonging to the forthcoming 4FGL catalog, whose publication is expected at the beginning of April 2018. 4FGL will be based on eight years of Fermi observations, thus providing a deeper and more complete description of the gamma-ray sky (more than 5500 sources will be included, compared to 3033 in 3FGL). Moreover, a much higher data quality will be guaranteed by the use of Pass 8 data, a new likelihood criterion to account for systematic errors, a new diffuse emission model and updated catalogs for multiwavelength associations. Future work will thus rely on new, better information to investigate the connection between neutrino and gamma-ray production in active galaxies and other kinds of sources.

Bibliography

[1] M. G. Aartsen et al. "Evidence for High-Energy Extraterrestrial Neutrinos at the IceCube Detector". In: *Science* 342 (2013), p. 1242856. DOI: 10.1126/science.1242856. arXiv: 1311.5238 [astro-ph.HE].

[2] M. G. Aartsen et al. "A combined maximum-likelihood analysis of the high-energy astrophysical neutrino flux measured with IceCube". In: *Astrophys. J.* 809.1 (2015), p. 98. DOI: 10.1088/0004-637X/809/1/98. arXiv: 1507.03991 [astro-ph.HE].

[3] M. G. Aartsen et al. "All-sky Search for Time-integrated Neutrino Emission from Astrophysical Sources with 7 yr of IceCube Data". In: *Astrophys. J.* 835.2 (2017), p. 151. DOI: 10.3847/1538-4357/835/2/151. arXiv: 1609.04981 [astro-ph.HE].

[4] M. G. Aartsen et al. "The contribution of Fermi-2LAC blazars to the diffuse TeV-PeV neutrino flux". In: *Astrophys. J.* 835.1 (2017), p. 45. DOI: 10.3847/1538-4357/835/1/45. arXiv: 1611.03874 [astro-ph.HE].

[5] B. P. Abbott et al. "Observation of Gravitational Waves from a Binary Black Hole Merger". In: *Phys. Rev. Lett.* 116 (6 Feb. 2016), p. 061102. DOI: 10.1103/PhysRevLett.116.061102. URL: https://link.aps.org/doi/10.1103/PhysRevLett.116.061102.

[6] B. P. Abbott et al. "GW170817: Observation of Gravitational Waves from a Binary Neutron Star Inspiral". In: *Phys. Rev. Lett.* 119 (16 Oct. 2017), p. 161101. DOI: 10.1103/PhysRevLett.119.161101. URL: https://link.aps.org/doi/10.1103/PhysRevLett.119.161101.

[7] A. A. Abdo et al. "Fermi Large Area Telescope First Source Catalog". In: ApJS 188 (June 2010), pp. 405–436. DOI: 10.1088/0067-0049/188/2/405. arXiv: 1002.2280 [astro-ph.HE].

[8] S. Abdollahi et al. "The second catalog of flaring gamma-ray sources from the Fermi All-sky Variability Analysis". In: *Astrophys. J.* 846.1 (2017), p. 34. DOI: 10.3847/1538-4357/aa8092. arXiv: 1612.03165 [astro-ph.HE].

[9] F. Acero et al. "Fermi Large Area Telescope Third Source Catalog". In: *Astrophys. J. Suppl.* 218.2 (2015), p. 23. DOI: 10.1088/0067-0049/218/2/23. arXiv: 1501.02003 [astro-ph.HE].

[10] W. B. Atwood et al. "The Large Area Telescope on the Fermi Gamma-Ray Space Telescope Mission". In: ApJ 697 (June 2009), pp. 1071–1102. DOI: 10.1088/0004-637X/697/2/1071. arXiv: 0902.1089 [astro-ph.IM].

[11] W. Atwood et al. "Pass 8: Toward the Full Realization of the Fermi-LAT Scientific Potential". In: *ArXiv e-prints* (Mar. 2013). arXiv: 1303.3514 [astro-ph.IM].

[12] J. Ballet et al. *Fermi-LAT 8-year Source List*. Online article. URL: https://fermi.gsfc.nasa.gov/ssc/data/access/lat/fl8y/FL8Y_description_v7.pdf (visited on 04/02/2018).

[13] ASI Space Science Data Center. *The Fermi LAT Third Source Catalog (3FGL)*. URL: http://www.ssdc.asi.it/fermi3fgl/ (visited on 04/01/2018).

[14] *Characterizing Diffuse Gamma-Ray Emission*. 2016. URL: https://fermi.gsfc.nasa.gov/science/eteu/diffuse/ (visited on 03/31/2018).

[15] Colin J. Clark et al. "Einstein@Home discovers a radio-quiet gamma-ray millisecond pulsar". In: *Science Advances* 4.2 (2018). DOI: 10.1126/sciadv.aao7228. eprint: http://advances.sciencemag.org/content/4/2/eaao7228.full.pdf. URL: http://advances.sciencemag.org/content/4/2/eaao7228.

[16] IceCube Collaboration. *GCN/AMON NOTICE*. Sept. 22, 2017. URL: https://gcn.gsfc.nasa.gov/notices_amon/50579430_130033.amon (visited on 04/01/2018).

[17] Charles Dennison Dermer and Berrie Giebels. "Active galactic nuclei at gamma-ray energies". In: *Comptes Rendus Physique* 17 (2016), pp. 594–616. DOI: 10.1016/j.crhy.2016.04.004. arXiv: 1602.06592 [astro-ph.HE].

[18] *Exploring Active Galactic Nuclei*. 2016. URL: https://fermi.gsfc.nasa.gov/science/eteu/pwn/ (visited on 03/31/2018).

[19] Ke Fang and Kohta Murase. "Linking High-Energy Cosmic Particles by Black Hole Jets Embedded in Large-Scale Structures". In: *Nature Physics* (2018). DOI: 10.1038/s41567-017-0025-4. arXiv: 1704.00015 [astro-ph.HE].

[20] *Fermi Searches for Dark Matter*. 2016. URL: https://fermi.gsfc.nasa.gov/science/eteu/dm/ (visited on 03/31/2018).

[21] R. C. Hartman et al. "The Third EGRET catalog of high-energy gamma-ray sources". In: *Astrophys. J. Suppl.* 123 (1999), p. 79. DOI: 10.1086/313231.

[22] IceCube Collaboration, E. Blaufuss, and C. Kopper. *GCN Circular 21916. IceCube-170922A - IceCube observation of a high-energy neutrino candidate event*. Sept. 23, 2017. URL: https://gcn.gsfc.nasa.gov/gcn3/21916.gcn3 (visited on 04/01/2018).

[23] IceCube Collaboration et al. "Neutrinos and Cosmic Rays Observed by IceCube". In: *ArXiv e-prints* (Jan. 2017). arXiv: 1701.03731 [astro-ph.HE].

[24] IceCube Collaboration, Fermi LAT Collaboration, et al. "Multiwavelength observations of a flaring blazar coincident with an IceCube high-energy neutrino". 2018. Submitted to *Science*.

[25] *Investigating Gamma-Ray Bursts*. 2016. URL: https://fermi.gsfc.nasa.gov/science/eteu/grbs/ (visited on 03/31/2018).

[26] *Investigating Pulsar Wind Nebulae*. 2016. URL: https://fermi.gsfc.nasa.gov/science/eteu/pwn/ (visited on 03/31/2018).

[27] G.F. Knoll. *Radiation Detection and Measurement*. Wiley, 2000. ISBN: 9780471073383.

[28] D. Kocevski et al. *Fermi All-Sky Variability Analysis (FAVA) - Source Report*. URL: https://fermi.gsfc.nasa.gov/ssc/data/access/lat/FAVA/SourceReport.php?week=477&flare=27 (visited on 04/01/2018).

[29] F. Krauß et al. "TANAMI blazars in the IceCube PeV-neutrino fields". In: A&A 566, L7 (June 2014), p. L7. DOI: 10.1051/0004-6361/201424219. arXiv: 1406.0645 [astro-ph.HE].

[30] Charles Meegan et al. "THE fermi gamma-ray burst monitor". In: *The Astrophysical Journal* 702.1 (2009), p. 791. URL: http://stacks.iop.org/0004-637X/702/i=1/a=791.

[31] P. F. Michelson, W. B. Atwood, and S. Ritz. "Fermi gamma-ray space telescope: High-energy results from the first year". In: *Rept. Prog. Phys.* 73 (2010), p. 074901. DOI: 10.1088/0034-4885/73/7/074901. arXiv: 1011.0213 [astro-ph.HE].

[32] *New Insights into Pulsar Physics*. 2016. URL: https://fermi.gsfc.nasa.gov/science/eteu/pwn/ (visited on 03/31/2018).

[33] *New Insights into SNRs from Fermi*. 2016. URL: https://fermi.gsfc.nasa.gov/science/eteu/snr/ (visited on 03/31/2018).

[34] P. L. Nolan et al. "Fermi Large Area Telescope Second Source Catalog". In: ApJS 199, 31 (Apr. 2012), p. 31. DOI: 10.1088/0067-0049/199/2/31. arXiv: 1108.1435 [astro-ph.HE].

[35] P. Padovani et al. "Active galactic nuclei: what's in a name?" In: *Astron. Astrophys. Rev.* 25.1 (2017), p. 2. DOI: 10.1007/s00159-017-0102-9. arXiv: 1707.07134 [astro-ph.GA].

[36] *Probing the Extragalactic Background Light*. 2016. URL: https://fermi.gsfc.nasa.gov/science/eteu/ebl/ (visited on 03/31/2018).

[37] *Spotting Terrestrial Gamma-Ray Flashes*. 2016. URL: https://fermi.gsfc.nasa.gov/science/eteu/tgfs/ (visited on 03/31/2018).

[38] M. Spurio. *Particles and Astrophysics: A Multi-Messenger Approach*. Springer International Publishing, 2015. ISBN: 9783319080505.

[39] Y. T. Tanaka, S. Buson, and D. Kocevski. "Fermi-LAT detection of increased gamma-ray activity of TXS 0506+056, located inside the IceCube-170922A error region." In: *The Astronomer's Telegram* 10791 (Sept. 2017).

[40] *The Enigmatic Class of Gamma-ray Binaries*. 2016. URL: https://fermi.gsfc.nasa.gov/science/eteu/binaries/ (visited on 03/31/2018).

[41] C. Megan Urry and Paolo Padovani. "Unified schemes for radio-loud active galactic nuclei". In: *Publ. Astron. Soc. Pac.* 107 (1995), p. 803. DOI: 10.1086/133630. arXiv: astro-ph/9506063 [astro-ph].

[42] M. Wood et al. *Fermi LAT Performance*. 2016. URL: http://www.slac.stanford.edu/exp/glast/groups/canda/lat_Performance.htm (visited on 03/31/2018).